

The Pennsylvania State University

The Graduate School

Graduate Program in Acoustics

**NOISE TRANSMISSION FROM A SMALL, HERMETIC, RECIPROCATING,  
REFRIGERANT COMPRESSOR**

A Thesis in

Acoustics

by

John Cunsolo

© 2018 John Cunsolo

Submitted in Partial Fulfillment  
of the Requirements  
for the Degree of

Master of Science

August 2018

The thesis of John Cunsolo was reviewed and approved\* by the following:

Timothy A. Brungart  
Research Professor, Graduate Program in Acoustics  
Thesis Co-Advisor

Stephen A. Hambric  
Research Professor, Graduate Program in Acoustics  
Thesis Co-Advisor

Daniel A. Russell  
Teaching Professor of Acoustics  
Director of Distance Education, Graduate Program in Acoustics

Victor W. Sparrow  
Professor of Acoustics  
Director of the Graduate Program in Acoustics

\*Signatures are on file in the Graduate School

## ABSTRACT

In recent years, refrigerant compressor design has become more focused on limiting the emission of noise, as many of these units are installed in residential spaces. This thesis aims to identify the primary transmission path of noise from a small, hermetic, reciprocating compressor to its enclosure; demonstrate the noise issues that result from its structural design; generate a procedure for a facilitated and accurate measurement of radiated sound power using structural acoustics theory; and evaluate a fundamental concept for attenuating mechanical noise. Measurements of transmissibility and radiated sound power of production line and rigidly-mounted units reveal that the mechanical transmission path dominates the shell excitation at frequencies critical to human hearing. Experimental modal analysis, shell mobility measurements, and sound power transfer function measurements show that the compressor mounts are located at antinodes of cylindrical shell modes with high radiation efficiency. A noise monitoring technique used to obtain radiated sound power of an operating compressor, given surface-averaged acceleration, is validated with measurements and promoted for use in monitoring structural design changes to products. A noise control concept is designed to decouple the suspension system from its compliant enclosure by grounding it to a rigid base, and it is successfully verified to attenuate the mechanical transmission path. The thesis concludes with possible future design implementations, as well as recommendations on how to reduce radiated noise from similar units.

# TABLE OF CONTENTS

<b>List of Figures.....</b>	<b>vi</b>
<b>List of Tables .....</b>	<b>x</b>
<b>List of Symbols .....</b>	<b>xi</b>
<b>Acknowledgements .....</b>	<b>xiv</b>
<b>Chapter 1</b>	
<b>Introduction.....</b>	<b>1</b>
<b>Chapter 2</b>	
<b>Methodology .....</b>	<b>6</b>
2.1 Design of Record.....	6
2.2 Radiated Sound Power .....	10
2.2.1 Theory.....	10
2.2.2 Measurement Procedure .....	12
2.3 Transmissibility .....	17
2.3.1 Theory.....	17
2.3.2 Measurement Procedure .....	19
2.4 Mobility .....	26
2.4.1 Single Degree-of-Freedom Mobility .....	26
2.4.2 Structural Mobility.....	27
2.4.3 Shells and the Ring Frequency .....	29
2.4.4 Drive Point and Surface-Averaged Mobility .....	30
2.4.5 Mobility Measurements .....	31
2.5 Experimental Modal Analysis .....	34
2.5.1 Cylindrical Mode Shapes.....	34
2.5.2 Measurement Procedure .....	35
2.6 Sound Power Transfer Function.....	37
2.6.1 Definition.....	37
2.6.2 Measurement Procedure .....	37
2.7 Radiation Efficiency.....	39
2.8 Radiation Loss Factor.....	40
2.9 Noise Monitoring .....	41
<b>Chapter 3</b>	
<b>Results &amp; Discussion.....</b>	<b>43</b>
3.1 Identifying the Dominant Transmission Path.....	43
3.1.1 Radiated Sound Power.....	43
3.1.2 Transmissibility .....	46
3.1.3 Comparing Radiated Sound Power and Transmissibility Levels.....	51
3.2 Characterizing the Shell Structure.....	53
3.2.1 Drive Point Mobility.....	53

3.2.2	Modal Analysis and Surface-Averaged Mount Mobility.....	55
3.2.3	Loss Factor.....	59
3.3	Effects of the Shell Structure on the Radiated Sound .....	60
3.3.1	Sound Power Transfer Function .....	60
3.3.2	Radiation Efficiency .....	61
3.3.3	Noise Monitoring.....	65
<b>Chapter 4</b>		
	<b>Noise Control.....</b>	<b>69</b>
4.1	Fundamental Design.....	69
4.2	Experimental Procedure .....	71
4.3	Results & Discussion.....	72
4.4	Spring Surging.....	77
<b>Chapter 5</b>		
	<b>Summary and Recommendations for Future Work .....</b>	<b>79</b>
<b>References</b>		

## LIST OF FIGURES

<i>Figure 1-1. Hermetic reciprocating refrigerant compressor provided by Bristol Compressors International, LLC.</i> .....	2
<i>Figure 2-1. Outer dimensions of refrigerant compressor model, normalized by mean cylindrical radius.</i> .....	7
<i>Figure 2-3. Simplified schematic of compressor unit with pictures of the compressor and the components that mount it to the enclosure.</i> .....	9
<i>Figure 2-4. Visual representation of microphone positions listed in Table 2-1 [5].</i> .....	14
<i>Figure 2-5. Radiated sound power level measurement setup in hemi-anechoic chamber.</i> .....	15
<i>Figure 2-6. Cutaway model of rigidly-mounted, operable compressor unit.</i> .....	17
<i>Figure 2-7. Transmissibility curves with varying damping ratios [8].</i> .....	19
<i>Figure 2-8. Inoperable compressor used for transmissibility testing.</i> .....	21
<i>Figure 2-9. Bottom mount arrangements for (a) design of record and (b) rigidly mounted conditions of transmissibility-tested compressor.</i> .....	22
<i>Figure 2-10. Aluminum fixture plate fabricated for transmissibility testing.</i> .....	24
<i>Figure 2-11. Accelerometer placement on the compressor unit. Vibration spectra were measured with a triaxial accelerometer at the crankcase (a) and with uniaxial accelerometers at the contact points of the mounting brackets and the lower housing (b).</i> .....	25
<i>Figure 2-12. Orientations of the compressor unit on the shaker and slip table. The compressor unit was shaken in the X (a), Y (b), and Z (c) directions, as indicated by each arrow.</i> .....	25
<i>Figure 2-13. Compressor unit instrumented with accelerometers, used for mobility measurements.</i> .....	32
<i>Figure 2-14. Hit point / measurement point grid for mobility measurements. Blue dots represent hit points; red dots represent accelerometer positions, which overlay eight of the hit points and are labeled as references. Points 17 and 23 are centered at the locations of the mounting brackets, while Point 89 is centered at the location of the stabilizer spring retainer.</i> .....	33
<i>Figure 2-15. Hit point / measurement point grid for modal analysis measurements. Blue dots represent hit points; red dots represent accelerometer positions, which overlay four of the hit points.</i> .....	36

<i>Figure 2-16. The same compressor shown in Figure 2-13, except the view is expanded to show the complete setup for sound power transfer function measurements. ....</i>	<i>38</i>
<i>Figure 3-1. Normalized radiated sound power spectrum of the design of record compressor unit in (a) narrow bands and (b) in one third octave bands. ....</i>	<i>44</i>
<i>Figure 3-2. A-weighting curve, commonly applied to sound power levels to give an accurate representation of how people perceive sound sources below 100 dB (unweighted). ....</i>	<i>45</i>
<i>Figure 3-3. Transmissibility of inoperable unit from enclosure at mounting brackets to compressor crankcase, forced and measured in the X direction, as indicated by the arrow. ....</i>	<i>47</i>
<i>Figure 3-4. Transmissibility of inoperable unit from enclosure at mounting brackets to compressor crankcase, forced and measured in the Y direction, as indicated by the arrow. ....</i>	<i>48</i>
<i>Figure 3-5. Transmissibility of inoperable unit from enclosure at mounting brackets to compressor crankcase, forced and measured in the Z direction, as indicated by the arrow. ....</i>	<i>49</i>
<i>Figure 3-6. Shock loop modes computed with finite element analysis. Peaks in the transmissibility of compressor assembly configurations with the shock loop installed correlate well with resonance frequencies of these modes. ....</i>	<i>51</i>
<i>Figure 3-7. Radiated sound power level (blue line) and transmissibility level (orange line) of rigidly mounted compressor minus those of the design of record unit, both in dB. Reference values are given in the legend. ....</i>	<i>52</i>
<i>Figure 3-8. Drive point mobility of eight measurement points on the compressor shell, as labeled in Figure 2-13, compared to trends of infinite plate, shell, and beam mobility as formulated by Cremer, Heckl, &amp; Ungar. Measurement points were split into those on the cylindrical portion (a) and those on the domal portion (b) of the enclosure, showing the influence of curvature on the low-frequency cut-on of shell mobility. ....</i>	<i>54</i>
<i>Figure 3-9. Cremer cylindrical shell modal estimates compared to shell modes found through modal analysis. ....</i>	<i>56</i>
<i>Figure 3-10. Surface-averaged mobility at mount locations with mode shapes compared to selected peaks. Two frequency ranges are displayed separately to show presence of beam modes (a) and cylindrical shell modes (b). The blue line is measured at position 17, the orange line is measured at position 23, and the yellow line is measured at position 89 (see Figure 2-13). ....</i>	<i>58</i>
<i>Figure 3-11. Loss factors calculated from modal analysis. The loss factors of the significant modes displayed in Figure 3-6 are identified with blue markers, and</i>	

<i>their mode shapes are placed beside them. The normalized critical (coincidence) frequency <math>\Omega_c = 0.418</math> is identified with a vertical black line. ....</i>	<i>59</i>
<i>Figure 3-12. Sound power transfer function computed from each accelerometer position. The normalized critical (coincidence) frequency <math>\Omega_c = 0.418</math> is identified with a vertical black line. ....</i>	<i>61</i>
<i>Figure 3-13. Surface-averaged mobility of the entire shell measured at each accelerometer position. The normalized critical (coincidence) frequency <math>\Omega_c = 0.418</math> is identified with a vertical black line. ....</i>	<i>62</i>
<i>Figure 3-14. Radiation efficiency measured at each accelerometer position, compared with the calculated Maidanik and Szechenyi curves, in (a) narrow bands and (b) one third octave bands. The normalized critical frequency <math>\Omega_c = 0.418</math> is identified with a vertical black line. ....</i>	<i>63</i>
<i>Figure 3-15. Sound power per surface-averaged vibration calculated at each position. ....</i>	<i>66</i>
<i>Figure 3-16. Normalized radiated sound power level in 0.39 Hz bands. The blue line was calculated from the averaged sound power transfer function, surface-averaged accelerance, and measured surface acceleration during operation. The orange line was measured in accordance with the ANSI/ISO 3745:2012 standard. ....</i>	<i>67</i>
<i>Figure 3-17. Normalized radiated sound power level in one third octave bands. The blue line was calculated from the averaged sound power transfer function, surface-averaged accelerance, and surface acceleration during operation. The orange line was measured in accordance with the ANSI/ISO 3745:2012 standard. ....</i>	<i>68</i>
<i>Figure 4-1. Transparent schematic of the windowed compressor fabricated for noise control testing. Acceleration spectra were measured with triaxial accelerometers at the shell enclosure (red square) and the compressor crankcase (blue square). The experiment was controlled with two uniaxial accelerometers on the rigid base (green circles). ....</i>	<i>70</i>
<i>Figure 4-2. Orientations of the rigid-base compressor on the shaker and slip table. The compressor was shaken in the X (a), Y (b), and Z (c) directions, as indicated by each arrow. ....</i>	<i>71</i>
<i>Figure 4-3. Attenuation in (a) 0.39 Hz bands and in (b) one third octave bands from the surface of the enclosure at the original bottom spring mount location to the compressor crankcase, forced and measured in the X direction. The blue line in each graph represents the design of record compressor measurements; the orange line represents those taken on the rigid base assembly. ....</i>	<i>74</i>
<i>Figure 4-4. Attenuation in (a) 0.39 Hz bands and in (b) one third octave bands from the surface of the enclosure at the original bottom spring mount location to the compressor crankcase, forced and measured in the Y direction. The blue line in each graph represents the design of record compressor measurements; the orange line represents those taken on the rigid base assembly. ....</i>	<i>75</i>

*Figure 4-5. Attenuation in (a) 0.39 Hz bands and in (b) one third octave bands from the surface of the enclosure at the original bottom spring mount location to the compressor crankcase, forced and measured in the Z direction. The blue line in each graph represents the design of record compressor measurements; the orange line represents those taken on the rigid base assembly.....*76

*Figure 4-6. Attenuation of rigid base assembly in Z-direction, compared to a 1-DOF model with spring surging resonances. ....*78

## LIST OF TABLES

<i>Table 2-1. Microphone positions for radiated sound power level measurement. ....</i>	13
---	----

## LIST OF SYMBOLS

$a$	Radius of cylindrical shell
$\bar{a}_c$	Acceleration magnitude
$a_{ell}$	Maximum radius of ellipse
$b_{ell}$	Minimum radius of ellipse
$C_1$	Reference sound power correction factor
$C_2$	Reference environment correction factor
$C_3$	Air absorption correction factor
$c_B$	Flexural wave speed
$c_l$	Longitudinal wave speed
$C_s$	Cylindrical shell circumference
$c_0$	Sound speed in air
$D$	Flexural rigidity
$d$	Damping coefficient
$d_c$	Critical damping coefficient
$E$	Real Young's Modulus
$F$	Complex, time-harmonic force
$\tilde{F}$	Complex force
$\bar{F}$	Force magnitude
$F_{in,mass}$	Force input at mass in a single degree-of-freedom vibrational system
$F_{out,base}$	Force output at base in a single degree-of-freedom vibrational system
$f$	Frequency
$f_c$	Critical (coincidence) frequency
$f_n$	Natural frequency
$G$	Shear modulus
$g$	Gravitational acceleration constant
$h$	Shell wall thickness
$\vec{I}$	Sound intensity vector
$I'$	Plate moment of inertia
$I_n$	Sample sound intensity for for far-field sound power
$K$	Shear correction factor
$k_s$	Helical wavenumber

$k_m$	Axial wavenumber
$k_n$	Circumferential wavenumber
$k_0$	Wavenumber in air
$L$	Length of cylindrical shell
$L_p$	Sound pressure level
$L_w$	Sound power level
$m_s$	Mass
$m_m$	Modal masses
$\vec{n}$	Unit vector
$\mathbf{p}$	Complex pressure
$\mathbf{P}_{\text{rad}}$	Radiated sound power
$P_{\text{ref}}$	Reference sound pressure
$\mathbf{P}_{\text{ref}}$	Reference sound power
$P_{\text{rms}}$	Root-mean-squared sound pressure
$r$	Sound power measurement radius
$r_T$	Ratio of frequency to natural frequency
$S_0$	Reference sound power surface area
$S_k$	Sample surface area per response point for surface-averaged mobility
$S_n$	Sample area for far-field sound power
$S_T$	Total measurement area for far-field sound power
$s$	Stiffness
$T$	Transmissibility
$t$	Time
$\vec{v}$	Complex particle velocity vector
$\tilde{v}$	Complex shell surface velocity
$\bar{v}$	Shell surface velocity magnitude
$W$	Weight of active coils of spring
$x$	Complex, time-harmonic displacement
$\dot{x}$	Complex, time-harmonic velocity
$\ddot{x}$	Complex, time-harmonic acceleration
$\tilde{x}$	Complex displacement
$x_{\text{mass}}$	Displacement of mass in a single degree-of-freedom vibrational system
$x_{\text{base}}$	Displacement of base in a single degree-of-freedom vibrational system

$\bar{x}_d$	Position of mobility drive point
$\bar{x}_v$	Position of mobility response point
$Y$	Mobility
$Y_{beam}$	Infinite beam mobility
$Y_{max}$	Maximum mobility
$Y_{plate}$	Infinite plate mobility
$Y_{shell}$	Infinite shell mobility
$z_0$	Characteristic impedance
$\Gamma_m$	Mode shapes
$\Delta f$	Half-power bandwidth
$\eta$	Structural loss factor
$\eta_{rad}$	Radiation loss factor
$\nu$	Poisson's ratio
$\rho_0$	Air density
$\rho_s$	Structural mass density
$\sigma$	Radiation efficiency
$\Omega$	Non-dimensionalized frequency
$\omega$	Angular frequency
$\Omega_c$	Non-dimensionalized critical frequency
$\omega_c$	Angular critical frequency
$\omega_m$	Angular modal frequencies
$\omega_n$	Angular natural frequency
$\tilde{\omega}_n$	Complex angular natural frequency
$\omega_{ring}$	Angular ring frequency

## ACKNOWLEDGEMENTS

Firstly, I would like to thank Bristol Compressors International, LLC., for sponsoring my M.S. degree, as well as for granting me the opportunity to work on a complex, challenging, and enjoyable problem to analyze and solve. I thank Dave Gilliam, in particular, for his oversight and collaboration on this project.

I would like to thank the research faculty and staff within the Applied Research Laboratory at Penn State University for their knowledge and assistance with this project. I thank James Chatterly for his direct involvement in setting up and taking measurements, as well as Zachary Yoas for familiarizing me with the measurement processes upon my arrival. I thank Dr. Benjamin Beck for providing his well-authored code to process the modal analysis data. Most of all, I thank Dr. Timothy Brungart and Dr. Stephen Hambric for advising me on my thesis, allowing me to further my career in acoustics and providing wisdom and resources to advance through this program and perform well in the industry.

I would like to thank the faculty and administration within the Graduate School of Acoustics for imparting their knowledge, wisdom, and resources during my time as an M.S. student. I thank Dr. Victor Sparrow for directing a world-renowned team of professors and scientists and encouraging his students to aim high in every aspect of their careers. I also thank Dr. Daniel Russell for providing me with valuable connections and mentoring me during some of the hardest times of this journey. His passion for acoustics, fueled by his love for the Lord, has inspired me to adopt pure ambitions and remain confident through every trial.

I would like to thank the community at Calvary Church, especially those at the Midtown campus, for welcoming me into State College with compassion and fellowship. Serving as worship leader and spending time with the pastors and staff have allowed me to learn more about myself and thrive in my field, as well as in every other aspect of my life.

Finally, I express gratitude towards my family and friends far away for their love and support. This thesis is dedicated to my parents and sister, James, Helen, and Gina Cunsolo. My work would not have seen completion without their prayers and encouragement.

“For the moment all discipline seems painful rather than pleasant, but later it yields the peaceful fruit of righteousness to those who have been trained by it.” Hebrews 12:11 ESV

# Chapter 1

## Introduction

The compressor is an integral part of the refrigeration cycle, which enables refrigerators and central air/water conditioning systems to operate. The compressor's primary function is to pressurize cooled, gaseous refrigerant and transfer it through the remainder of the system. When it reaches the condenser, the high-pressure gas is passed through a coil that is cooled with air or water, and it changes to a liquid state. Then, the refrigerant flow rate is restricted as it is fed through a metering device, consequently reducing the pressure. The cool, liquid refrigerant passes through the coils of an evaporator; this unit supplies cool air to the surrounding environment and returns warm air, which heats up the coils, thereby changing the state of the refrigerant from liquid to gas. As the fluid reenters the compressor, this cycle is repeated.

The device, shown in Figure 1 and used in this study, is a small hermetic compressor, provided by Bristol Compressors International, LLC. A hermetic compressor is sealed airtight inside a steel, cylindrical shell. Compressors in this category are typically mounted onto their enclosures with isolating springs. This product is also categorized as a reciprocating compressor for its method of processing refrigerant. A motor rotates a crankshaft, causing two pistons to move laterally, out of phase with one another. Refrigerant enters the compressor by means of the suction inlet. The pistons compress the refrigerant by opening space for it to flow into the crankcase and pushing it into the cylinder head, thus adding pressure to the refrigerant and increasing its temperature. The compressed refrigerant travels along a path leading it through the discharge tube and out of the enclosure.



*Figure 1-1. Hermetic reciprocating refrigerant compressor provided by Bristol Compressors International, LLC.*

The reciprocating compression process generates the noise that is perceived by the consumer. The most noticeable peaks in the noise spectrum are typically found at the rotational frequency of the pistons and its harmonics. It is commonly advised to manufacturers not to design a vibration isolation system with a fundamental frequency that matches that of the motor rotation rate frequency or any of its harmonics, as these resonances will become more pronounced.

One common issue found with hermetic, reciprocating compressor noise comes from the low-order acoustic cavity resonances of the enclosure. A cavity resonance occurs due to the

residual volume of an enclosure, much like an acoustic room mode. Tested and approved changes to address this issue include moving the locations of the suction and discharge valves to nodal regions, or places within the cavity that experience minimal sound pressure [1], and oil foaming to reduce fluid pressure inside the cavity [2].

By far the most troubling issue with hermetic, reciprocating compressors is the overall increase in sound pressure due to the structural resonances of the enclosure. As mentioned previously, the vibration isolation system is mounted directly to the shell; as a result, the compressor drives the shell as it operates, and the mechanically borne noise is amplified at the shell's structural resonances. These shell modes cause the most significant noise issues for small compressors, as the most strongly radiating modes are found within the frequency range to which the human ear is the most sensitive [2]. If the compressor is mounted to the shell at antinodes, places where the structural modes are most active, then these resonances can be clearly heard.

Means have been devised to reduce such mechanically transmitted noise. Changing the shape of the shell to represent more of a sphere than a cylinder has been shown to reduce noise at critical listening frequencies, as spherical shell resonances are higher and more susceptible to coupling losses [3]. One common solution proven to attenuate noise is applying viscoelastic damping to the shell at antinodes of the structural modes of the enclosure; this method is commonly executed by applying a layer of dissipating polymer and a constraining steel layer on top [4]. Some experiments have shown that the flange, or the lap joint, bonding the top and bottom housing pieces of the enclosure can be moved toward the node of highly radiating shell modes, since thicker shells are stiffer and more efficient radiators of sound, and resonances of the shell can be shifted to higher frequencies and away from the critical range of human hearing [1].

However, there are two noise control solutions that have been proposed in the literature that have not been validated as thoroughly as the others. Waser and Hamilton suggest stiffer spring mounts to reduce mobility of the shell at lower frequencies [4], while Hamilton also

recommends relocating the spring mounts of the vibration isolation system to nodal regions of shell modes [2]. Little is known about the validity of these approaches to the noise control problem; therefore, given the design of the specific compressor provided by Bristol, this thesis will explore the possibility of implementing these solutions.

The purpose of this thesis is to identify the primary transmission path(s) of noise from a small, hermetic, reciprocating compressor to its shell enclosure by studying the mechanical vibration isolation system and corresponding trends in vibration transmissibility and radiated sound power. The thesis aims to demonstrate the noise issues that result from its structural design using experimental modal analysis and surface mobility measurements. It will use structural acoustics theory to validate a procedure for a facilitated and accurate measurement of radiated sound power that allows a manufacturer to calculate radiated sound power of a hermetic compressor given the surface acceleration of the shell. Finally, the thesis will propose a fundamental solution to the noise issue with a design that mounts the compressor's vibration isolation onto a more rigid base, decoupling it from the shell.

In the Methodology section, the structural design and functions of the specific compressor unit provided for this thesis are given in detail. The procedures for each measurement of surface vibration, modal analysis, radiated sound power, and the sound power transfer function are outlined with information on the measurement standards and the acoustics theory used.

In the Results section, the general radiated sound spectra of the operating compressor is presented, leading into a diagnostics study to determine the primary transmission path of noise. Important transmissibility testing results will be shown suggesting that the mechanical transmission path plays a primary role in the radiation of noise. Drive point vibration is compared to an infinite structure mobility model to identify the cut on and cut off of shell modes. Mode shapes from the modal analysis confirm the presence of these cylindrical shell modes and reveal the locations of antinodes near the spring mounts. Loss factors are shown and related to radiation

efficiency curves. Radiated sound power transfer functions, radiation efficiencies, and sound power per surface averaged vibration are calculated and presented at various reference locations on the shell.

In the Noise Control section, an effort is demonstrated to mitigate mechanically transmitted noise through the vibration isolation system of the compressor unit. An assembly, designed with a compressor mounted with springs onto a rigid base and structurally decoupled from its enclosure, is fabricated and tested with the same procedure as the transmissibility testing. Attenuation across the mounts of the unit designed for noise control is compared to that of the design of record unit; a significant improvement in the performance of the vibration isolation is shown. Furthermore, the results are compared to a single degree-of-freedom model with spring surging to shed light on another phenomenon to consider in limiting the mechanical transmission path.

Finally, this thesis concludes with a section summarizing the effort and its primary findings. It will discuss the application of structural acoustics experimental procedures to industrial product testing. This section will also provide recommendations for future work related to the compressor unit used in this study.

# Chapter 2

## Methodology

### 2.1 Design of Record

The product used for this study, shown in Figure 1, is a small, hermetic, reciprocating, refrigerant compressor, produced by Bristol Compressors International, LLC. Figure 2-1 shows a drawing of the outer dimensions of the unit, normalized by the mean radius of the cylindrical enclosure. Some important dimensions of the unit, expressed as ratios, will be used for calculated estimates of structural properties of the cylindrical portion of the enclosure. For instance, the ellipse ratio (maximum radius to minimum radius ratio) is 1.34, the height to mean radius ratio is 3.56, and the ratio of the wall thickness to mean radius is 0.03.

Figure 2-2 gives an exploded view of the complete assembly of the operable compressor used for this study. As low-pressure refrigerant enters the compressor (40), it is suctioned into the cylinder head (21). A motor drives a crankshaft (9), which oscillates two pistons (26) 180° out of phase with one another; together, the pistons pressurize the refrigerant at an operating frequency of  $\Omega = 7.553 \cdot 10^{-4}$ , as given in Figure 2-1. The gas is then discharged through the carbon steel muffler (22), the stainless steel shock loop (6), and out of the compressor through the discharge tube (7).

The steel upper and lower housings (38 and 1) are lap welded together, forming the enclosure that seals the compressor unit gastight. Rubber mounting grommets (43) support the unit at the holes of its mounting feet (2) and provide ground isolation; it is assumed, then, that the enclosure has free structural boundary conditions on the top and bottom. Apart from its complex geometry designed to conform to the shape of the compressor inside, the housing is essentially an

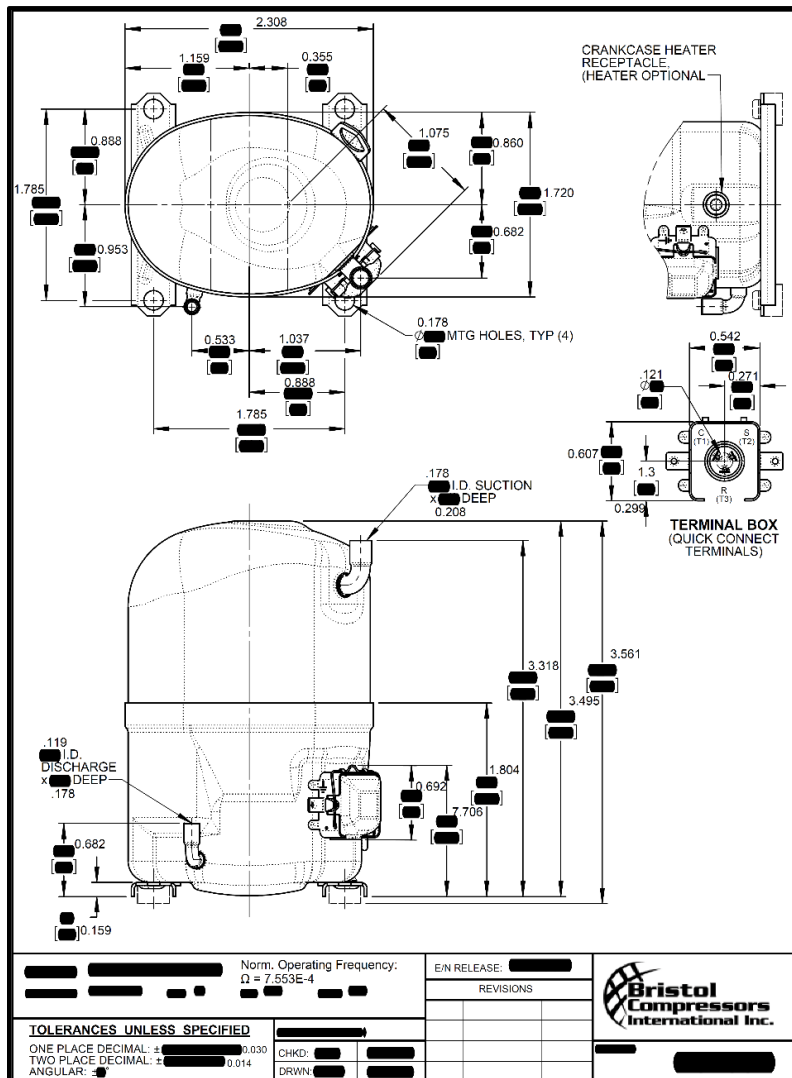


Figure 2-1. Outer dimensions of refrigerant compressor model, normalized by mean cylindrical radius.

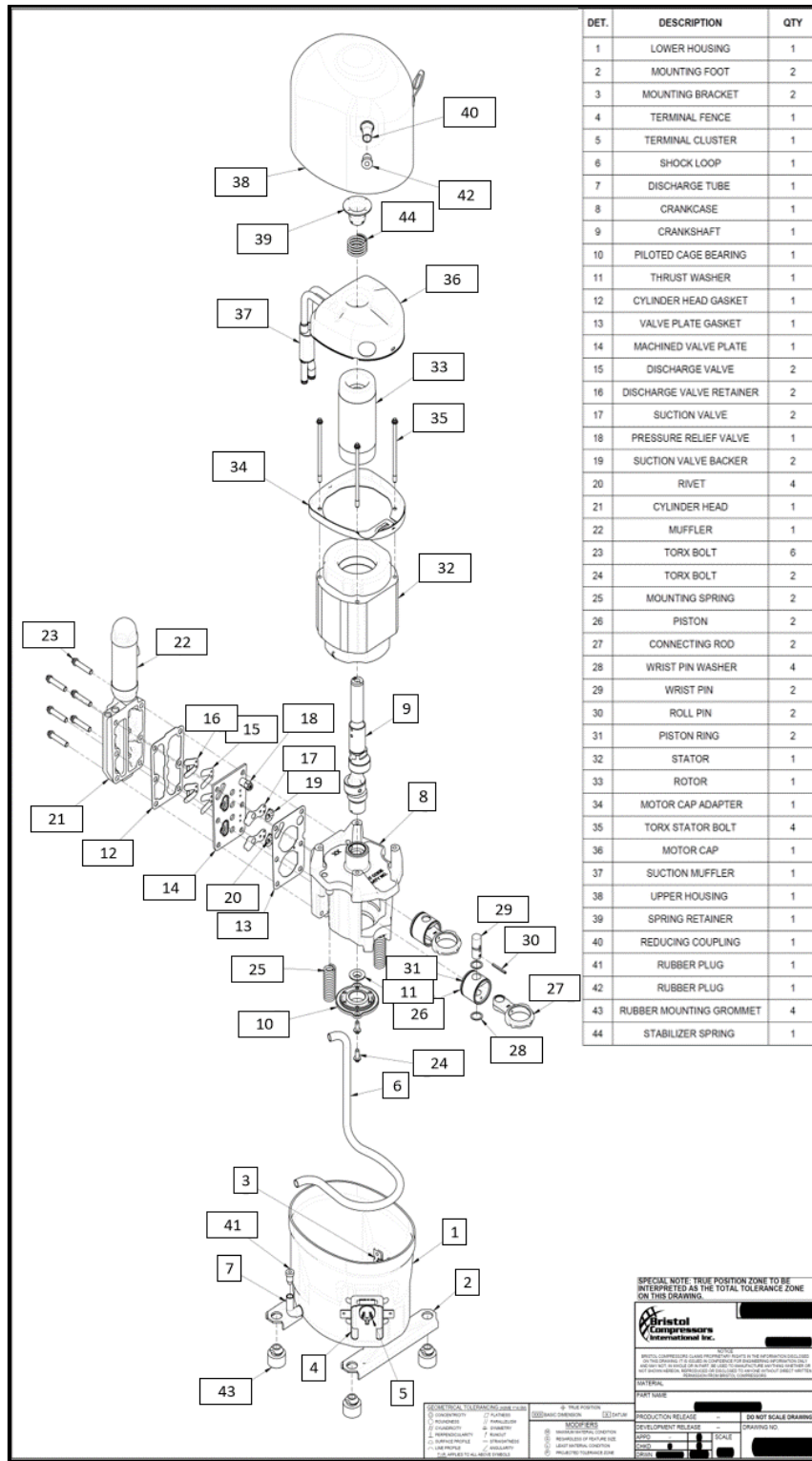
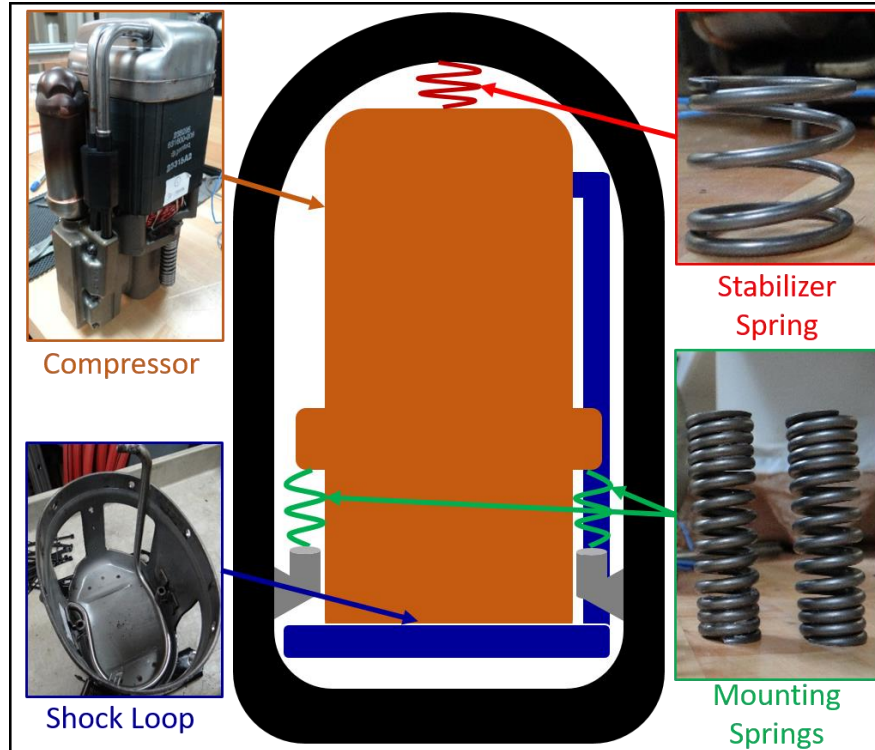


Figure 2-2. Exploded view of refrigerant compressor.

elliptical cylindrical shell with domed top and bottom ends. Therefore, upon analyzing the structural properties of the enclosure, one should expect similar properties of a cylindrical shell to be present.

The compressor has springs on its top and bottom purposed for vibration isolation. It is mounted at either side of the crankcase (8) upon two mounting (bottom) springs (25), which sit upon mounting brackets (3) pressed and welded onto the inner, cylindrical walls of the lower housing. A stabilizer (top) spring (44) sits in between the compressor's motor cap (36) and a spring retainer (39) pressed and welded onto the inner surface of the upper housing.

Figure 2-3 shows a simplified schematic of the unit with pictures of the compressor, the stabilizer spring, the mounting springs, and the shock loop. The springs and the shock loop ground the compressor to its enclosure; therefore, these elements of the unit were studied in evaluating the performance of the vibration isolation system.



**Figure 2-3. Simplified schematic of compressor unit with pictures of the compressor and the components that mount it to the enclosure.**

## 2.2 Radiated Sound Power

### 2.2.1 Theory

As an object vibrates, its surface pushes on the particles of the surrounding fluid medium, creating waves that propagate outward. In general, the sound intensity is defined as:

$$\vec{I} = \frac{1}{2} \text{Re}\{\mathbf{p}\vec{v}^*\}, \quad (2-1)$$

where  $\mathbf{p}$  and  $\vec{v}$  are the complex pressure and particle velocity vector, respectively. In the far field, the pressure and particle velocity are in phase and are related by the characteristic impedance of the medium  $z_0$ , such that  $\frac{\mathbf{p}}{v} = z_0 = \rho_0 c_0$ , where  $\rho_0$  and  $c_0$  are the density and sound speed of the surrounding fluid, respectively. Thus, the far field intensity is given by:

$$\vec{I} = \frac{|\mathbf{p}|^2}{\rho_0 c_0}. \quad (2-2)$$

Equation (2-2) is only true for plane and spherical waves. For sources that do not radiate sound equally in all directions, such as cylindrical surfaces, it is necessary to measure the far-field sound intensity of the same source over sample areas in multiple directions.

The radiated sound power of all sound sources is defined by:

$$\mathbf{P}_{\text{rad}} = \iint_{S_T} \vec{I} \cdot \vec{n} dS_T, \quad (2-3)$$

where  $\vec{n}$  is the unit vector normal to the radiating surface and  $S_T$  is the area over which the intensity is measured. Using  $N$  far-field intensity measurements  $I_n$  of the same source, the radiated sound power of a directional source may be approximated as

$$\mathbf{P}_{\text{rad}} = \sum_{n=1}^N I_n S_n, \quad (2-4)$$

where  $S_n$  is a sample area, over which its corresponding intensity  $I_n$  is measured.

As a receiver moves farther away from the acoustic source, the observed sound intensity decreases, because the power generated by the source is radiated over a larger area. In a half-free space environment, where a sound source sits on a reflecting surface in a hemi-anechoic room, the area of the sound pressure field observed is  $S_T = 2\pi r^2$ , where  $r$  is the distance from the source. When spherical spreading of sound is assumed, the acoustic intensity and the surface area of the observed medium are inversely proportional to one another in the far field; in this ideal case, the radiated sound power is independent of  $r$ .

The sound pressure level  $L_P$  is a logarithmic metric of the sound pressure, expressed in decibels (dB). This metric is commonly reported in acoustical applications with a reference sound pressure level  $P_{\text{ref}}$ , which represents the threshold of human hearing; in air, this value is equal to  $20 \mu\text{Pa}$ . The sound power level  $L_W$  is a logarithmic metric of the sound power with a reference sound power level  $\mathbf{P}_{\text{ref}}$  of  $10 \text{ pW}$ . Each are commonly expressed as

$$L_P = 20 \cdot \log_{10} \left( \frac{|P_{rms}|}{P_{ref}} \right); \quad (2-5)$$

$$L_W = 10 \cdot \log_{10} \left( \frac{P_{\text{rad}}}{P_{\text{ref}}} \right). \quad (2-6)$$

### ***2.2.2 Measurement Procedure***

The radiated sound power level of an operable compressor was obtained using the ANSI/ASA S12.55-2012 / ISO 3745:2012 standard, which prescribes measurements of sound pressure in both anechoic and hemi-anechoic rooms. Complying with the “general case” of measuring sound power in a hemi-anechoic room, as described by the standard, the sound pressure was measured with microphones placed in a hemispherical pattern at a radius of 1 meter. Table 2-1 [5], taken directly from the standard text, lists the coordinates of each measurement position, normalized by the radius of the hemisphere. Note that the x/r and y/r dimensions of positions 21-40 mirror those of positions 1-20 across the x and y axes; to satisfy this condition, one measurement was taken with microphones placed in the first 20 positions, and another measurement was taken with the sound source rotated 180° to capture the sound pressures at the second 20 positions. A visual representation of the 20-microphone arrangement, taken directly from the standard, is presented in Figure 2-4 [5].

*Table 2-1. Microphone positions for radiated sound power level measurement [5].*

<b>Position Number</b>	$x/r$	$y/r$	$z/r$
1	-1.000	0.000	0.025
2	0.499	-0.864	0.075
3	0.496	0.859	0.125
4	-0.492	0.853	0.175
5	-0.487	-0.844	0.225
6	0.961	0.000	0.275
7	0.000	0.947	0.325
8	-0.803	-0.464	0.375
9	0.784	-0.453	0.425
10	0.762	0.440	0.475
11	-0.737	0.426	0.525
12	0.000	-0.818	0.575
13	0.781	0.000	0.625
14	-0.369	0.693	0.675
15	-0.344	-0.596	0.725
16	0.316	-0.547	0.775
17	0.283	0.489	0.825
18	-0.484	0.000	0.875
19	0.000	-0.380	0.925
20	0.192	0.111	0.975
21	1.000	0.000	0.025
22	-0.499	0.864	0.075
23	-0.496	-0.859	0.125
24	0.492	-0.853	0.175
25	0.487	0.844	0.225
26	-0.961	0.000	0.275
27	0.000	-0.947	0.325
28	0.803	0.464	0.375
29	-0.784	0.453	0.425
30	-0.762	-0.440	0.475
31	0.737	-0.426	0.525
32	0.000	0.818	0.575
33	-0.781	0.000	0.625
34	0.369	-0.693	0.675
35	0.344	0.596	0.725
36	-0.316	0.547	0.775
37	-0.283	-0.489	0.825
38	0.484	0.000	0.875
39	0.000	0.380	0.925
40	-0.192	-0.111	0.975

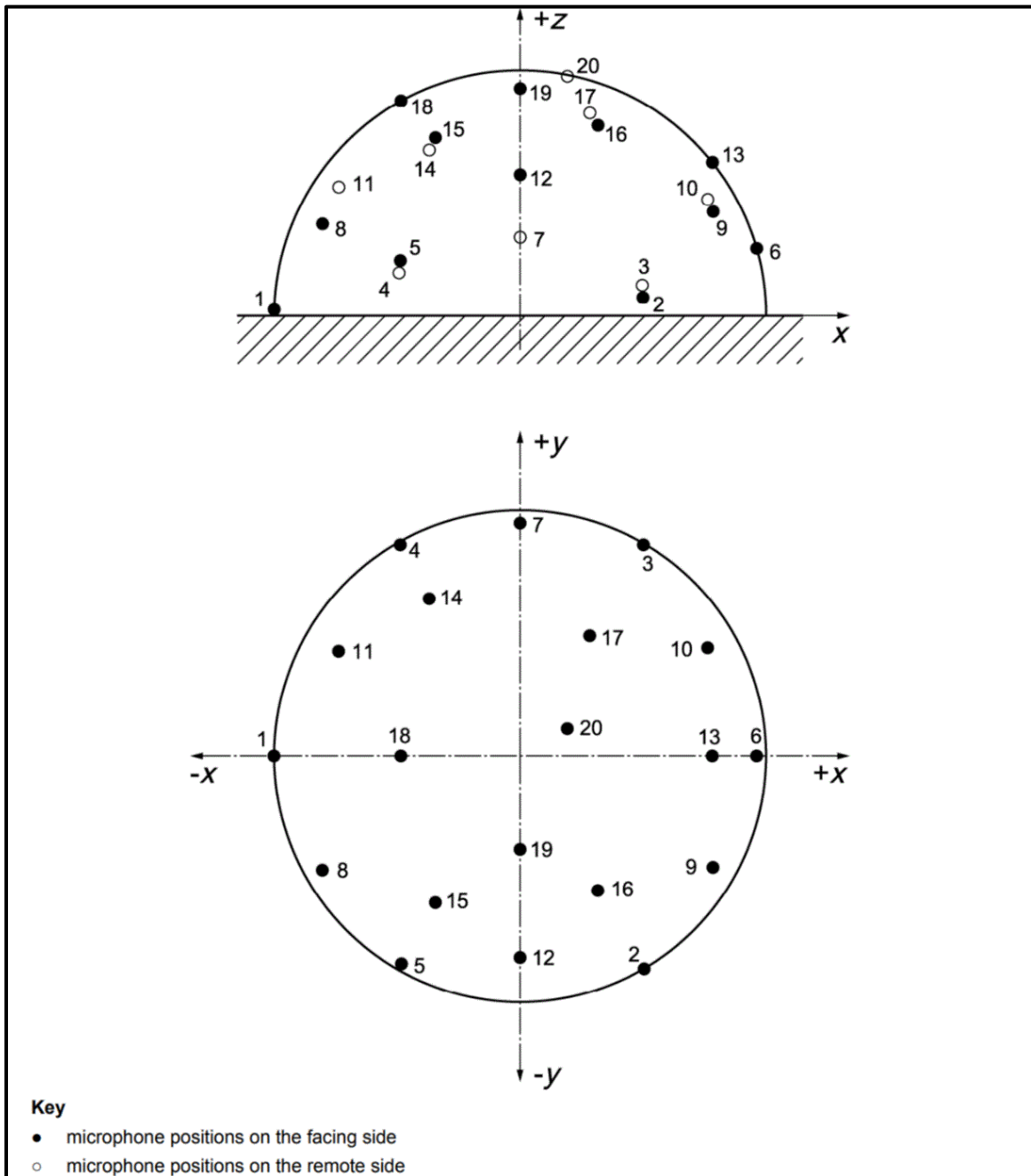


*Figure 2-4. Visual representation of microphone positions listed in Table 2-1 [5].*

Figure 2-5 shows the compressor and the microphone setup in the middle of the ARL Penn State Flow-Through Anechoic Chamber. This chamber has a cutoff frequency of 70 Hz, a working volume of 9.3 m height x 5.5 m width x 6.8 m depth, and fiberglass wedges lined along

all the internal surfaces, minus the floor [6]. Twenty ½” PCB 378A06 condenser microphones were plugged into an NI-3034x Data Acquisition system and set up on a custom-built pole array. The compressor was set to run with an inlet temperature of 50°F and an outlet temperature of 115°F. Using software custom-built in LABVIEW, one minute of time history data of the sound pressure was collected at a sampling frequency of 51200 Hz; then, the compressor was rotated 180°, and another minute of sound pressure data was collected. The steady state temperature, humidity, and barometric pressure of the room were also recorded at the time of the test. The time history data collected was then processed using a Hanning window and a Fast Fourier Transform (FFT) to calculate the linear spectrum of pressure. The pressure was averaged over time, as well as over all 40 measurement positions, and the sound pressure level  $L_p$  was calculated using Equation (2-5).



*Figure 2-5. Radiated sound power level measurement setup in hemi-anechoic chamber.*

Following the standard, the sound power level was calculated by the following [5]:

$$L_W = L_p + 10 * \log_{10} \left( \frac{S_T}{S_0} \right) + C_1 + C_2 + C_3, \quad (2-7)$$

where

$S_T$  is the surface measurement area, in square meters;

$S_0$  is the reference measurement area, = 1 m<sup>2</sup>;

$C_1$  is a correction factor<sup>a</sup> that adjusts for both the reference sound pressure and the reference sound power in air;

$C_2$  is a correction factor<sup>b</sup> used to account for the temperature and static pressure of the testing room, in order to report the sound power of the source in a reference-based environment;

$C_3$  is a correction factor<sup>c</sup> for air absorption due to the air temperature, humidity, and static pressure.

In addition to the sound power of a design-of-record operable compressor unit, the sound power of a rigidly mounted operable compressor unit was also tested. Figure 2-6 shows a schematic of this assembly. The springs and mounting brackets were exchanged for steel blocks bolted to the mount locations in order to provide hard connections between the compressor and its enclosure. The measurements taken to compare the radiated sound power levels of these two compressor units were performed by Bristol, in accordance with the ANSI/AHRI Standard for Rating of Sound and Vibration for Refrigerant Compressors (530-2011) [7]. The purpose of

---

<sup>a</sup> For an air temperature of 26 °C and static air pressure of 109 kPa, the correction factor  $C_1 = -0.42$  dB.

<sup>b</sup> For an air temperature of 26 °C and static air pressure of 109 kPa, the correction factor  $C_2 = -0.64$  dB.

<sup>c</sup> For an air temperature of 26 °C, static air pressure of 109 kPa, and relative air humidity of 50%, the correction factor  $C_3(1000 \text{ Hz}) = -0.006$  dB.

comparing the radiated sound power of a production-line compressor unit with a rigidly mounted case was to evaluate the performance of the vibration isolation system.

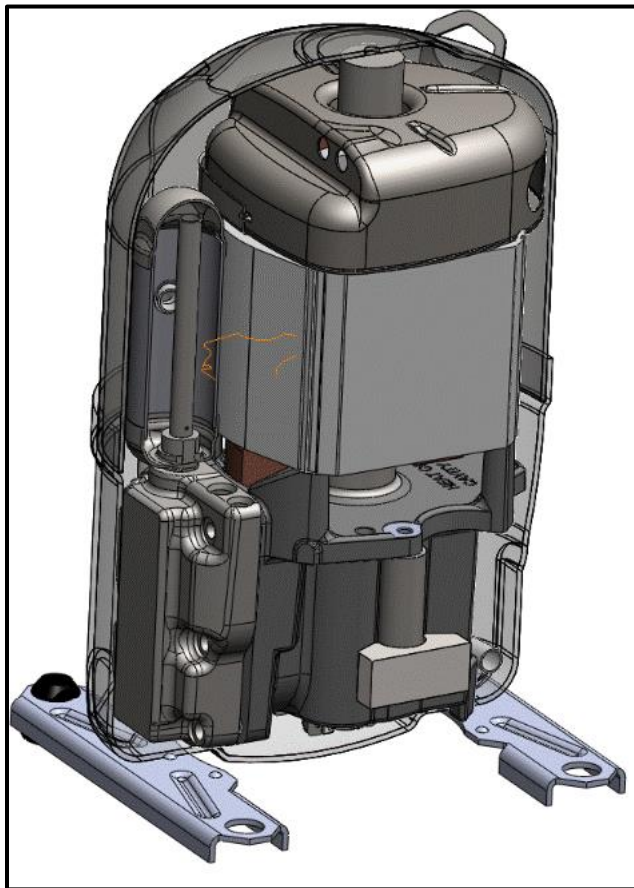


*Figure 2-6. Cutaway model of rigidly-mounted, operable compressor unit.*

## 2.3 Transmissibility

### 2.3.1 Theory

The *transmissibility* of a vibrational mass-spring-damper system grounded to a base is its output-to-input ratio. This quantity is usually defined in two ways:

$$T = \left| \frac{F_{out,base}}{F_{in,mass}} \right|_{x_{base}=0} = \left| \frac{x_{mass}}{x_{base}} \right|_{F_{in,mass}=0}, \quad (2-8)$$

where  $F_{out,base}$  is the force transmitted to the base,  $F_{in,mass}$  is the force directly applied to the mass,  $x_{mass}$  is the displacement of the mass, and  $x_{base}$  is the displacement of the base [8]. At any given angular frequency  $\omega$ , the transmissibility of a single degree-of-freedom (1-DOF) system with stiffness  $s$ , mass  $m_s$ , and damping coefficient  $d$  can be determined from

$$T = \frac{\sqrt{1 + (2\xi r_T)^2}}{\sqrt{(1 - r_T^2)^2 + (2\xi r_T)^2}}, \quad (2-9)$$

where the damping ratio  $\xi = \frac{d}{d_c} = \frac{d}{2m_s\omega_n}$ ,  $r_T = \frac{\omega}{\omega_n}$ , and the angular resonance frequency

$\omega_n = \sqrt{\frac{s}{m_s}}$ . The damping ratio is defined as the level of damping compared to that required for critical damping, or the lowest level of damping that suppresses a vibrational system to the point of preventing oscillation. Figure 2-7 shows transmissibility curves that occur with given damping ratios [8]. A characteristic transmissibility curve will have a value of 1 at very low frequencies, followed by a peak that amplifies the response at and near the resonance frequency of the system. This amplification changes with the system's level of damping. Above the fundamental resonance, transmissibility will decrease logarithmically with increasing frequency, but it will increase with increased damping.

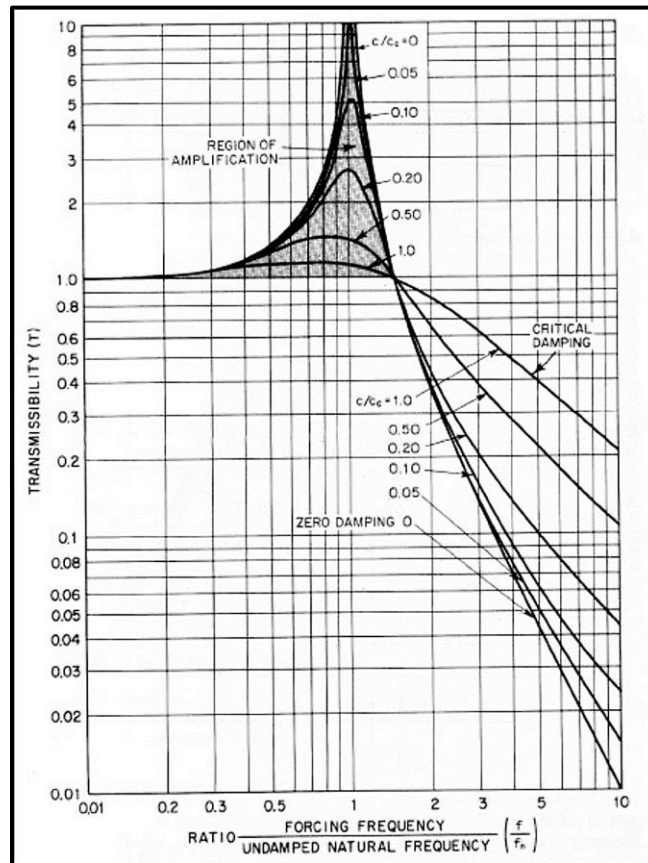


*Figure 2-7. Transmissibility curves with varying damping ratios [8].*

### 2.3.2 Measurement Procedure

Concerns about the vibration isolation were raised upon analyzing the structural design of the unit. While the springs are in place to keep the compressor from transmitting vibration to its enclosure, both the top and bottom spring mounts couple the compressor to parts of a steel enclosure that are relatively thinner than an ideal rigid foundation for a mass-spring system. It should also be noted that the shock loop, which channels the high-pressure gas to the discharge valve and provides additional rocking stability, is brazed to the compressor's muffler at its top end and welded onto the housing at its bottom end. This direct coupling can also create a flanking

path that bypasses isolating springs and facilitates the mechanical transmission of compressor-generated noise to a radiating shell. Thus, it was deemed necessary to study the effectiveness of the vibration isolation and the influence of the mechanical transmission path on noise radiated from the compressor unit.

A special assembly was prepared for the purpose of measuring the transmissibility between the compressor and its enclosure at each end of one of the bottom springs, shown in Figure 2-8. Surfaces on the compressor's crankcase were smoothed for accelerometer placement. Rectangular windows (indicated by blue arrows) were cut into the upper and lower housings in order to make it easier to place accelerometers inside the enclosure. Holes (indicated by green arrows) were tapped and threaded into the overlap portions of the upper and lower housings so that these sections of the enclosure may be bolted together, allowing the upper housing to be removed. Finally, metal eyebolts (indicated by red arrows) were screwed into the corners of the upper housing to facilitate transportation of the unit. As a result of these alterations, the assembly used for transmissibility testing was inoperable.

These modifications also permitted the replacement and exclusion of specific parts of the general assembly. In some cases, the stabilizer spring was exchanged with a more compliant model, and in other cases it was removed altogether. The mounting springs were also switched out with those of roughly half their stiffness in a sample of cases. In addition to these alterations, a second lower housing was prepared without the shock loop welded on, and almost all the same cases for the springs were performed with this base. Although these components are considered essential to the operation of the compressor, they were exchanged and/or removed for the purpose of studying their effects on the mechanical transmission path between the compressor and its enclosure.



*Figure 2-8. Inoperable compressor used for transmissibility testing.*

Then, a rigidly mounted case was explored with the transmissibility tests. Much like with the radiated sound power tests, the goal of this configuration was to remove the influence of the springs and the shock loop and evaluate the performance of the complete vibration isolation system compared to a case with hard connections between the compressor and its foundation.

Figure 2-9 shows pictures of the bottom mounts of the design of record and rigidly mounted configurations.

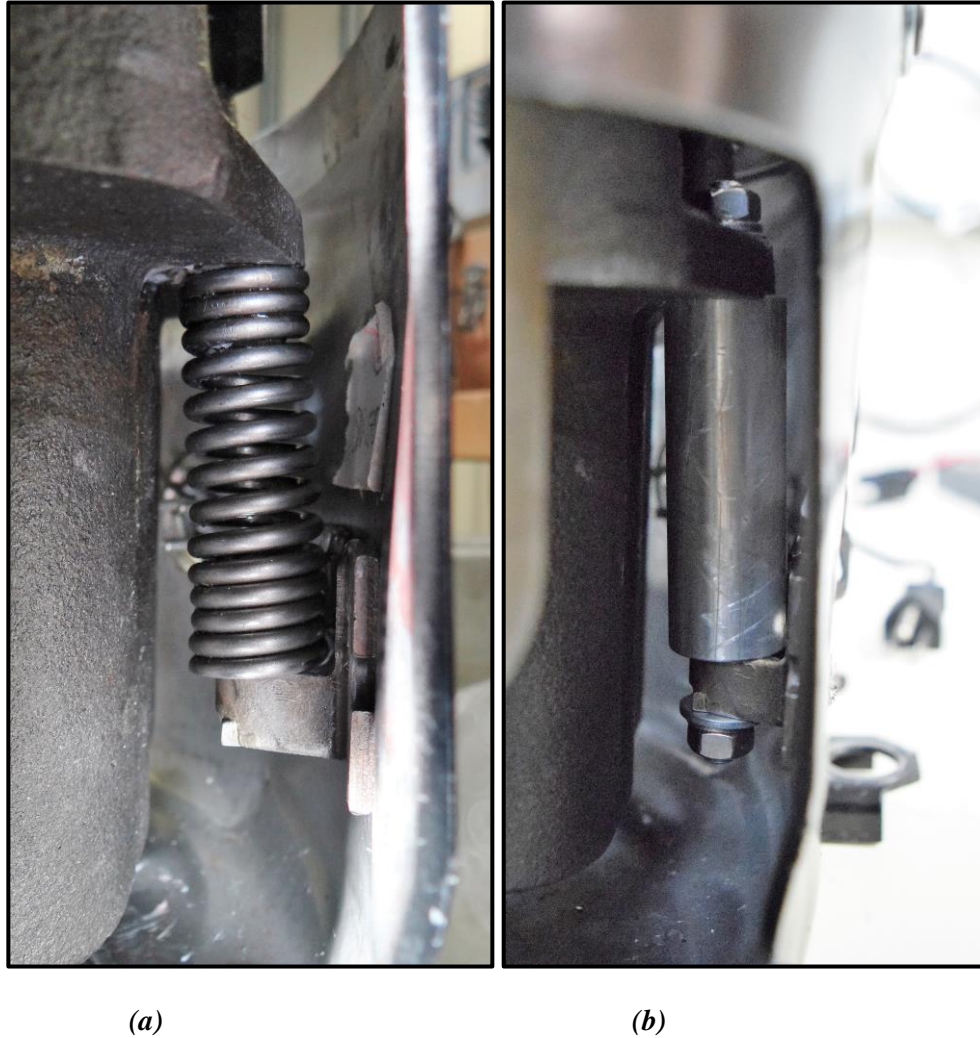


***Figure 2-9. Bottom mount arrangements for (a) design of record and (b) rigidly mounted conditions of transmissibility-tested compressor.***

Finally, the differences in performance between the design of record case and its rigidly mounted counterpart were compared to one another (radiated sound power level of operable units and transmissibility of inoperable units), in order to find a correlation between the radiated noise of the unit and the mechanical transmission path from the compressor to its foundation. A few

disparities between the rigidly mounted assemblies used were that 1) the operable compressor had a fully hermetic enclosure, while the enclosure for the inoperable compressor had windows; 2) the operable compressor had a hard mount in place of the stabilizing spring, while the inoperable compressor had no top mount in place of said spring; 3) the operable compressor was bolted to custom-made, thicker mounting brackets, while the inoperable compressor was bolted to the design-of-record mounting brackets; and 4) the operable compressor had the shock loop installed, while the inoperable compressor did not.

The inoperable unit was shaken with an Unholtz Dickie ST Series Slip Table Assembly. A special fixture plate, shown in Figure 2-10, was crafted to affix the compressor unit to the shaker and the slip table. Four holes were threaded to bolt the legs of the compressor to the fixture, and 21 holes were tapped in a radial pattern in order to bolt the fixture to the shaker and the slip table. Figure 2-11 shows the placement of the accelerometers on the assembly. Uniaxial accelerometers (PCB W352C677) were placed on the compressor enclosure close to the points of contact with the mounting brackets. Using mounting cubes, the accelerometers were oriented in line with the axis of each forced oscillation. These accelerometers controlled the input force, meaning that a feedback loop was used to fix the response of the shell at the accelerometer locations to a given function. A triaxial accelerometer (PCB 356A32) was placed on the crankcase of the compressor, atop the point of connection with one of the mounting springs. Another triaxial accelerometer was mounted on the bottom of the mounting bracket, but the spectra taken at the control accelerometers were preferred over that taken at the bracket, in order that the complete path from the compressor to the enclosure may be taken into account. Figure 2-12 shows the orientations of the compressor unit on the shaker and the table. Arrows indicate the directions in which the compressor unit was shaken and the vibration spectra were measured. An input of random noise from 5 to 5000 Hz with maximum amplitude of 2 times

gravitational acceleration was given to excite the assembly. Time history data, sampled at 51200 Hz, was collected for 3 minutes of this excitation for each test.



*Figure 2-10. Aluminum fixture plate fabricated for transmissibility testing.*

One important principle was used for the transmissibility testing. During operation of a standard unit, the compressor itself generates mechanical noise, which is then conducted through the mounting system to the enclosure. During transmissibility testing, the enclosure was mechanically excited, and the response at the compressor was deemed the output. As discussed in Section 2.3.1, transmissibility can be defined either as a ratio of output force at the base to force applied at the mass or as a ratio of output mass displacement to input base displacement. This relationship allowed for the measurement of transmissibility from the shell mount to the compressor.

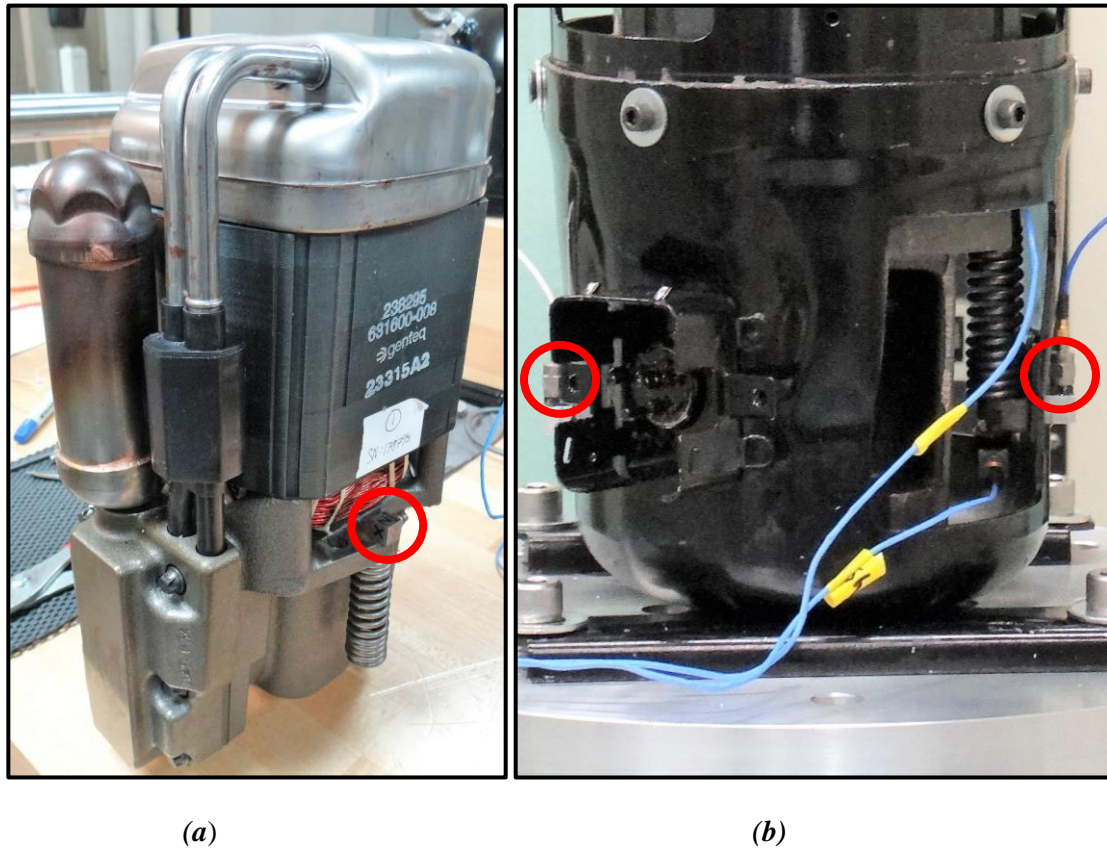


*Figure 2-11. Accelerometer placement on the compressor unit. Vibration spectra were measured with a triaxial accelerometer at the crankcase (a) and with uniaxial accelerometers at the contact points of the mounting brackets and the lower housing (b).*

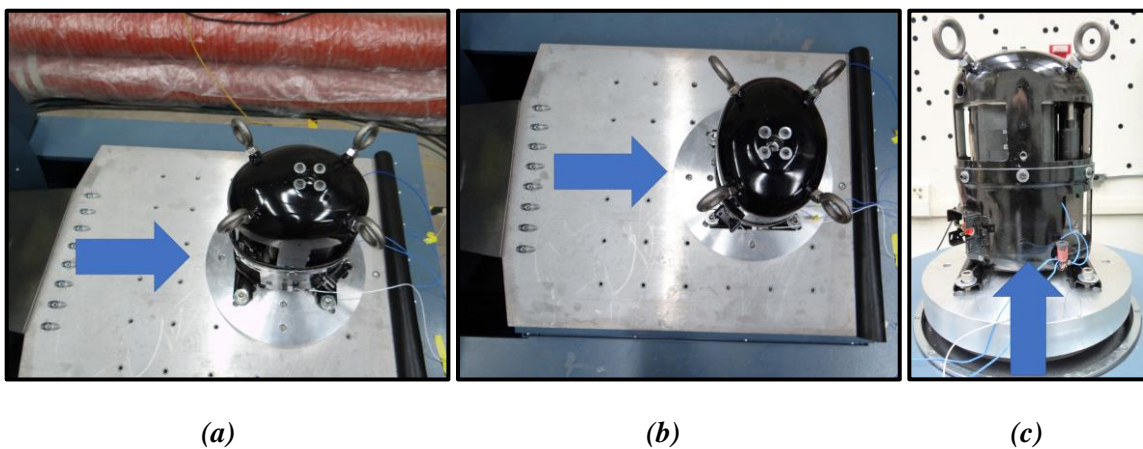


*Figure 2-12. Orientations of the compressor unit on the shaker and slip table. The compressor unit was shaken in the X (a), Y (b), and Z (c) directions, as indicated by each arrow.*

## 2.4 Mobility

### 2.4.1 Single Degree-of-Freedom Mobility

A force  $F$  acts upon a 1-degree-of-freedom (1-DOF) system with mass  $m_s$ , stiffness  $s$ , and damping  $d$ , causing the system to respond with a displacement  $x$ . This system can be described using a differential equation [9]

$$m_s \ddot{x} + d\dot{x} + sx = F, \quad (2-10)$$

where  $\dot{x}$  is the velocity, defined as the first derivative of  $x$  with respect to time  $t$ , and  $\ddot{x}$  is the acceleration, defined as the second derivative of  $x$  with respect to time. Assuming the force and displacement are time harmonic, where  $F(t) = \tilde{F}e^{i\omega t}$  and  $x(t) = \tilde{x}e^{i\omega t}$ , and substituting into Equation (2-10) gives

$$-\omega^2 m_s \tilde{x} + i\omega d \tilde{x} + s \tilde{x} = \tilde{F}, \quad (2-11)$$

where  $\tilde{F}$  and  $\tilde{x}$  are the complex force and displacement, respectively. By factoring out  $\tilde{x}$  and isolating it with  $\tilde{F}$ , the equation becomes

$$\frac{\tilde{x}}{\tilde{F}} = \frac{1}{(-\omega^2 m_s + i\omega d + s)}. \quad (2-12)$$

The complex velocity  $\tilde{v}$  of the system in the frequency domain is equal to  $i\omega\tilde{x}$ . By scaling each side of Equation (2-12) by  $i\omega$ , neglecting viscous damping in the system, and solving the

expression of angular resonance frequency  $\omega_n$  for  $k$ , a convenient expression for mobility of a simple harmonic oscillator is found:

$$\tilde{Y} = \frac{\tilde{v}}{\tilde{F}} = \frac{i\omega}{m_s(\omega_n^2 - \omega^2)}. \quad (2-13)$$

*Mobility* is the response of a vibrational system to an oscillating force, where the output is a measured velocity. The response of the signal is greatest at the resonance frequencies of the vibrational system, when  $\omega = \omega_n$ . It should be noted that by increasing the moving mass, the mobility of the system decreases.

#### 2.4.2 Structural Mobility

While a single degree-of-freedom, mass-spring-damper system shares the same location of driving force and response, structures have multiple degrees of freedom that are coupled to one another. It is necessary, therefore, to take into account a response at any point  $\bar{x}_v$  to a drive at any point  $\bar{x}_d$  and incorporate a modal summation in determining mobility of a structure as a function of frequency. The following equation gives the general case for structural mobility [10]

$$\frac{\tilde{v}(\bar{x}_v)}{\tilde{F}(\bar{x}_d)} = \sum_{m=1}^N \left( \frac{i\omega}{m_m} \frac{\Gamma_m(\bar{x}_v, \bar{x}_d)}{(\omega_m^2 - \omega^2)} \right). \quad (2-14)$$

The mode shapes  $\Gamma_m$  at points  $\bar{x}_v$  and  $\bar{x}_d$  have an influence on how a structure responds to a point force when excited at its modal resonance frequencies  $\omega_m$ . The structure has an effective modal mass  $m_m$  for each mode shape; for a simply supported plate, the modal mass is

constant for all modes and equivalent to a quarter of the total mass of the plate. One can select a peak mode order  $N$  of modes to incorporate in the sum. Depending on the structure, more mode orders may be needed for the solution to converge to a particular mobility curve.

As seen in Equation (2-11), inclusion of damping in a vibrational system makes the modal frequencies and shapes complex. As opposed to viscous damping, structural damping requires a relation to displacement, not velocity; therefore, it is directly applied to the elastic properties of the system. Structural damping can be incorporated through the introduction of a complex stiffness

$$\frac{\tilde{x}}{\tilde{F}} = \frac{1}{(-\omega^2 m_s + (1 + i\eta)s)}, \quad (2-15)$$

where  $\eta$  is the structural loss factor. Given the half-power bandwidth  $\Delta f$  of the peak-normalized, magnitude-squared mobility  $\left| \frac{Y}{Y_{max}} \right|^2$  at resonance frequency  $f_n$ , the structural loss factor  $\eta \cong \frac{\Delta f}{f_n}$ .

The natural angular frequency  $\omega_n$  becomes the complex angular frequency  $\tilde{\omega}_n$

$$\tilde{\omega}_n = \sqrt{\frac{(1 + i\eta)s}{m_s}} \cong \omega_n \left( 1 + i \frac{\eta}{2} \right). \quad (2-16)$$

Structural losses can then be applied to the general case of structural mobility

$$\frac{\tilde{v}(\bar{x}_v)}{\tilde{F}(\bar{x}_d)} = \sum_{m=1}^N \left( \frac{i\omega}{m_m} \frac{\Gamma_m(\bar{x}_v, \bar{x}_d)}{(\tilde{\omega}_m^2 - \omega^2)} \right). \quad (2-17)$$

### 2.4.3 Shells and the Ring Frequency

In structural acoustics problems involving shells, the non-dimensionalized frequency  $\Omega$  is often used. This value is simply  $\omega$  normalized by the ring frequency  $\omega_{ring}$ , which is the frequency at which a longitudinal wave with speed  $c_l$  can propagate around the circumference  $C_s$  of a cylindrical shell [11]. Given the real Young's modulus  $E$ , Poisson's ratio  $\nu$ , and mass density  $\rho_s$  of the shell material, the complex longitudinal wave speed  $c_l$  is expressed as

$$c_l = \sqrt{\frac{E(1+i\eta)}{(1-\nu^2)\rho_s}}. \quad (2-18)$$

The second Ramanujan approximation for the circumference of an ellipse [12] was used to estimate the ring frequency of the cylindrical part of the enclosure of the compressor:

$$\omega_{ring} = 2\pi \left( \frac{c_l}{C_s} \right); \quad (2-19a)$$

$$C_s \approx \pi(a_{ell} + b_{ell}) \left( 1 + \frac{3s}{10 + \sqrt{4 - 3s}} \right); \quad (2-19b)$$

$$s = \frac{(a_{ell} - b_{ell})^2}{(a_{ell} + b_{ell})^2}, \quad (2-19c)$$

where  $a_{ell}$  is the maximum radius and  $b_{ell}$  is the minimum radius.

#### 2.4.4 Drive Point and Surface-Averaged Mobility

The *drive point mobility* is found when the drive and response locations are the same ( $\bar{x}_v = \bar{x}_d$ ). Measuring drive point mobility is particularly helpful in determining what types of structural modes to look for in a complex structure at different frequency ranges. For instance, the drive point mobility of a structure with a finite-length cylindrical shell will behave similarly to an infinite-length beam at low frequencies, an infinite-area plate at high frequencies, and an infinite-length shell somewhere in between. Using infinite structure theory, Cremer, Heckl, and Ungar approximated these behaviors and their cutoffs for a cylindrical shell of inner radius  $a$ , thickness  $h$ , and density  $\rho_s$  [13]

$$\operatorname{Re}\{Y_{beam}\} = \left[ 4\pi a \rho_s h \sqrt{\frac{\Omega c_l^2}{\sqrt{2}}} \right]^{-1}, \quad \Omega < 0.77 \frac{h}{a}; \quad (2-20a)$$

$$\operatorname{Re}\{Y_{shell}\} = \frac{0.66}{2.3 c_l \rho_s h^2} \sqrt{\Omega}, \quad 0.77 \frac{h}{a} < \Omega < 0.6; \quad (2-20b)$$

$$Y_{plate} = \frac{1}{8\sqrt{D\rho_s h}}, \quad \Omega > 0.6; \quad (2-20c)$$

where the flexural rigidity  $D = \frac{Eh^3(1+i\eta)}{12(1-\nu^2)}$ . Because the cross section of the cylindrical portion of the compressor enclosure is elliptical, the mean of the maximum radius  $a_{ell}$  and the minimum radius  $b_{ell}$  was used as the value for  $a$ .

The *surface-averaged mobility* is the response of an entire surface to a driving force, normalized by the total area of the surface. This form of mobility is useful for determining how the mode shapes will influence the response of the structure as a whole or in one particular

section. Given one drive point, the mobility magnitude at each one of  $M$  response points is scaled by a sample area  $S_k$ ; the products are then summed and averaged by the sum of the sample areas, or the total surface area. Equation 21 expresses the surface-averaged mobility as a function of angular frequency

$$\left\langle \left| \frac{v}{F(\bar{x}_d)} \right| \right\rangle (\omega) = \sum_{k=1}^M \frac{\left| \sum_{m=1}^{\infty} \left( \frac{i\omega}{m_m} \frac{\Gamma_m(\bar{x}_{v,k}, \bar{x}_d)}{(\tilde{\omega}_m^2 - \omega^2)} \right) \right| dS_k}{\sum_{k=1}^M dS_k}. \quad (2-21)$$

The principle of vibrational reciprocity states that the transfer mobility, or the mobility of a system in which the drive and response locations are not the same, remains the same when these locations are swapped. Therefore, it is acceptable to measure the response at one point to the force at several drive points, one at a time, and use these mobility magnitudes to calculate and interpret the surface-averaged mobility as the response of the entire surface to a force at the measurement point.

#### 2.4.5 *Mobility Measurements*

Mobility testing was performed on an operable compressor unit, which was placed in a hemi-anechoic chamber and set for operation in the same manner as the radiated sound power testing, seen in Figure 2-13. A grid of lines was drawn onto the enclosure, and 100 drive points were selected. Because of limited accessibility to the bottom of the enclosure, the mobility testing was limited to points on the cylindrical shell and the top of the enclosure. The unit was charged with refrigerant, and the enclosure was instrumented with eight PCB W352C677 uniaxial accelerometers, each weighing 2 g, glued onto the shell at eight of the 100 drive points. It was

unverified whether mass loading from the accelerometers would skew the measurements. Three of these accelerometers were placed on points coinciding with the locations of the compressor mounts (two near the mounting brackets on the sides and one near the stabilizer spring retainer on top). Figure 2-14 shows the locations of the hit points in blue and the accelerometers in red. A PCB 086C03 impact hammer with a metal tip was used to create a force impulse on each drive point. Ten averages, each 2.56 seconds long, of time history data of the force and acceleration were collected at a sampling frequency of 51200 Hz with an NI-3034x Data Acquisition system and custom-built software. Another set of software computed the mobility spectra of the data.



*Figure 2-13. Compressor unit instrumented with accelerometers, used for mobility measurements.*

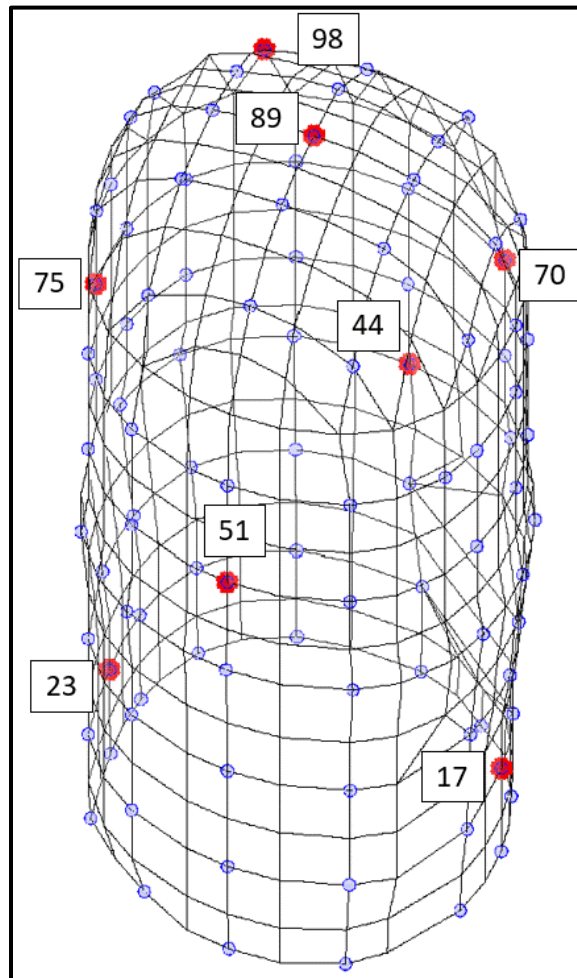


***Figure 2-14. Hit point / measurement point grid for mobility measurements. Blue dots represent hit points; red dots represent accelerometer positions, which overlay eight of the hit points and are labeled as references. Points 17 and 23 are centered at the locations of the mounting brackets, while Point 89 is centered at the location of the stabilizer spring retainer.***

This measurement procedure served multiple purposes in this study. The drive point mobility of the compressor shell was calculated at all eight accelerometer locations to determine the frequency ranges of beam, shell, and plate mobility behavior. The surface-averaged mobility was computed over the surface areas covering each of the three mount locations; if these direct connections to the shell laid within antinodal regions of structural mode shapes, then peaks in the surface-averaged mobility would coincide with the modal frequencies of these mode shapes.

Finally, the surface-averaged mobility of the entire structure was computed at each accelerometer position and used to process measurements of the sound power transfer function, discussed in Section 2.2.5.

## 2.5 Experimental Modal Analysis

### 2.5.1 Cylindrical Mode Shapes

Mode shapes are an important component of the mobility of a structure. Much like standing waves on a string have nodes (points with minimum displacement) and antinodes (points with maximum displacement), mode shapes have nodal and antinodal regions with minimum and maximum mobility, respectively; depending on where the structure is excited, it may respond well or poorly to the driving force. Each mode shape is stimulated at its own resonance frequency; while exact solutions for these mode shapes are tedious to produce analytically, the resonance frequencies can be approximated for various simple structures. For example, Cremer et al. estimated the resonance frequencies of cylindrical shell radial modes [13] with

$$\Omega_{m,n}^2 = \frac{\omega_{m,n}^2}{\omega_{ring}^2} \cong \frac{k_m^4}{k_s^4} + \beta^2 \left[ k_s^4 a^4 - \frac{n^2(4-\nu) - 2 - \nu}{2(1-\nu)} \right], \quad (2-22)$$

where

$k_s = \sqrt{k_m^2 + k_n^2}$ , the helical wavenumber;

$k_m = m\pi/2L$ , the axial wavenumber for simply supported boundary conditions;

$m = 1, 2, 3, \dots$ , the axial mode order;

$k_n = n/a$ , the circumferential wavenumber;

$n = 0, 1, 2, 3, \dots$ , the circumferential mode order;

$\beta^2 = h^2 / 12a^2$ ; and  $L$  is the length of the cylindrical shell.

### **2.5.2 Measurement Procedure**

For the refrigerant compressor unit used for this study, *experimental modal analysis* was performed to obtain the modal characteristics of the mass and fluid-loaded enclosure. This process involves obtaining the response of the outer structure, at a select number of accelerometer locations, to a measured force at a vast number of drive points. Again, using vibrational reciprocity, it is assumed that these transfer mobilities can be interpreted as responses at the drive points to forces at the accelerometer locations. Observing the frequency response curves of these mobilities and breaking each one down into many single degree-of-freedom systems will yield the resonance frequencies, mode shapes, and loss factors. At each modal frequency, the imaginary part of the mobility determines the mode shapes, while the real part of the mobility determines the damping of the system.

The same operable compressor unit was used for this measurement as the one for surface mobility; from the same grid, 391 points were selected, shown in Figure 2-15. The upgrade in the number of hit points was considered in order to obtain the highest-order mode shapes as possible for comparison to Cremer's mode estimates. The unit was charged with refrigerant, and the enclosure was instrumented with four PCB W352C677 uniaxial accelerometers, glued onto the shell at four of the drive points. A PCB 086C03 impact hammer with a metal tip was used to create a force impulse on each drive point. The metal tip was used to obtain as high of a frequency range of modes as possible. Three averages, each 2.56 seconds long, of time history data of the force and acceleration were collected at a sampling frequency of 51200 Hz with an NI-3034x Data Acquisition system and custom-built software. A CAD model of the compressor

was used to build the geometry of the mesh with the selected drive points in order to produce accurate mode shapes. Another set of software implemented an automated peak extraction method to process the measurements, allowed the user to select modes from the mobility data, and computed the mode shapes of the shell at each resonance frequency.

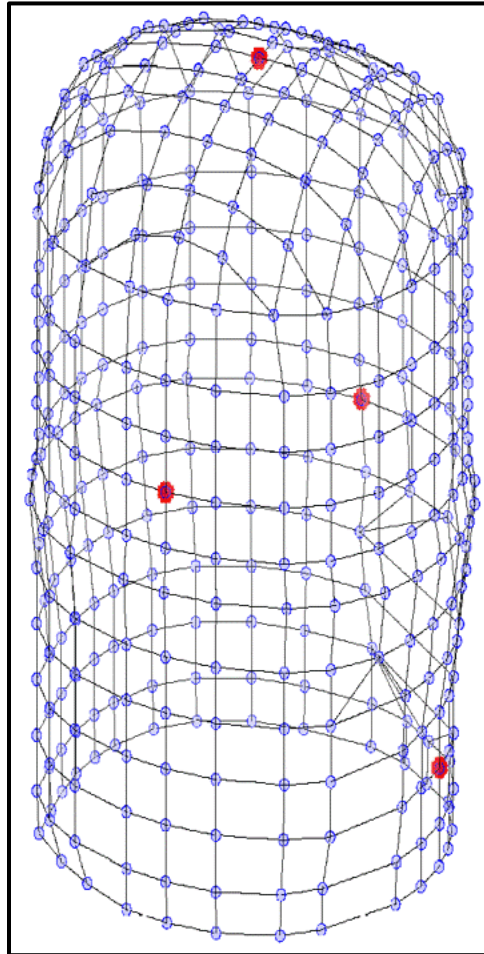


*Figure 2-15. Hit point / measurement point grid for modal analysis measurements. Blue dots represent hit points; red dots represent accelerometer positions, which overlay four of the hit points.*

## 2.6 Sound Power Transfer Function

### 2.6.1 Definition

The *sound power transfer function* is defined here as the radiated sound power  $\mathbf{P}_{\text{rad}}$  of a source, given the mean squared force  $\bar{F}^2$  applied to its surface. This transfer function is useful in determining how the structural characteristics of the radiating surface affect the sound spectrum observed in the surrounding fluid medium; major peaks in the transfer function identify structural modes that radiate well. It is broken down into three important components, shown by the following [14]:

$$\frac{\mathbf{P}_{\text{rad}}}{\bar{F}^2} = \frac{\langle |\bar{v}|^2 \rangle}{\bar{F}^2} \frac{\mathbf{P}_{\text{rad}}}{\rho_0 c_0 S_T \langle |\bar{v}|^2 \rangle} \rho_0 c_0 S_T , \quad (2-23)$$

where the first term in blue is the squared, surface-averaged mobility; the second term in red is the sound power radiation efficiency  $\sigma$ ; and the third term in green is the characteristic mechanical fluid impedance. A simple way of obtaining the sound power transfer function is to measure the vibro-acoustic transfer function, defined as the sound pressure of a radiating surface due to an impact force on that surface, at several far-field measurement points. Each transfer function is substituted for  $\mathbf{p}$  in Equation (2-2), and the same process is used as in Equation (2-4) to obtain the radiated sound power as a function of the mean squared force.

### 2.6.2 Measurement Procedure

The sound power transfer function of the operable compressor unit was measured in the same setting as the surface mobility. Figure 2-16 displays the complete setup with the compressor standing inside the microphone array. The compressor was set up inside the hemispherical

microphone array used for radiated sound power testing; the impact hammer was also used as an input force source. A metal tip was used to acquire data as high above 1000 Hz as possible; a rubber tip was used to obtain a sufficient response above the noise floor, without damaging the shell, at frequencies below 1000 Hz. The drive force was measured at 100 points on the shell, and the pressure response to each hit was measured at the 20 microphone positions used for radiated sound power testing. Ten 2.56-second averages were recorded at each drive point. The goal of this measurement was to obtain the sound power transfer function using a well-documented, ANSI/ISO standard of measuring sound power.

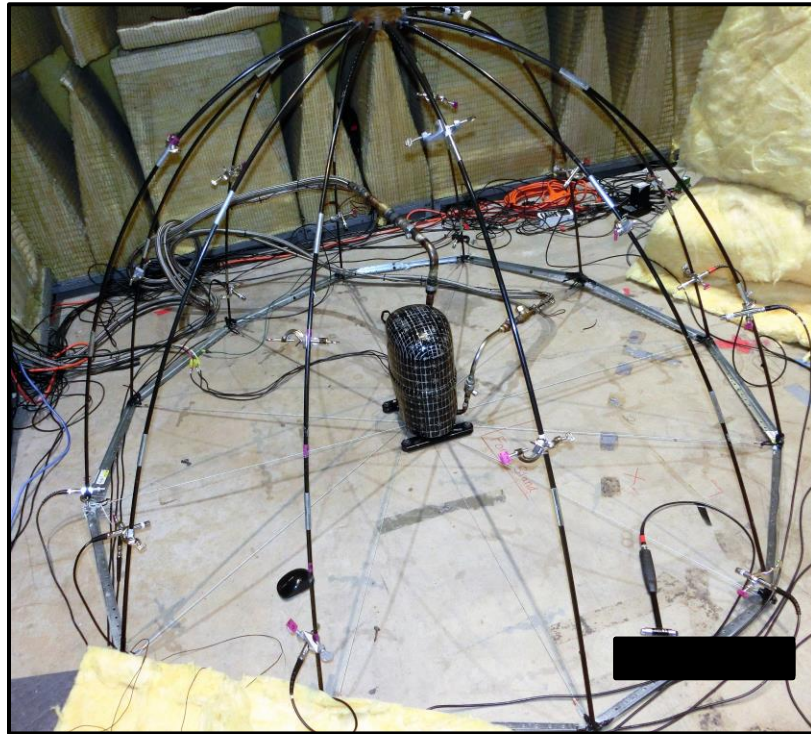


*Figure 2-16. The same compressor shown in Figure 2-13, except the view is expanded to show the complete setup for sound power transfer function measurements.*

## 2.7 Radiation Efficiency

The *radiation efficiency*, shown in red in Equation (2-23), is defined here as the ratio of the sound power of a realistic source to that of a simply supported radiating piston in an infinite baffle. Typically, the behavior of a structure's radiation efficiency depends on the acoustic and structural wave speeds. Unlike the wave speed in a fluid, which generally stays constant with frequency, the flexural wave speed of a plate with thickness  $h$ , structural mass density  $\rho_s$ , and flexural rigidity  $D$  changes with frequency [15]

$$c_B = \sqrt{\frac{\sqrt{(A_1 - A_2)^2 \omega^4 + 4A_3 \omega^2} - \omega^2(A_1 + A_2)}{2(1 - \omega^2 A_4)}}; \quad (2-24)$$

$$A_1 = \frac{D}{KhG}; A_2 = \frac{I'}{h}; A_3 = \frac{D}{\rho_s h}; A_4 = \frac{I' \rho_s}{KhG},$$

where  $K$  is the shear correction factor (5/6 for plates, similar for shells),  $G$  is the shear modulus of the material, and  $I'$  is the moment of inertia about the normal axis for a plate ( $h^3/12$ ). The frequency at which  $c_B = c_0$  is the structure's critical (coincidence) frequency, where  $\omega_c = 2\pi f_c$  and  $c_0$  is the wave speed in air. At low frequencies,  $c_B < c_0$ , and sound will radiate poorly; at high frequencies,  $c_B > c_0$ , and  $\sigma = 1$ . At the critical frequency,  $\sigma$  is at its highest, and it is primarily controlled by the amount of damping in the system. For less flexible, less dense structures, the critical frequency is lowered, making the radiation efficiency rise. The flexural wave speed is computed without effects of fluid loading, which lower the speed of flexural waves, so it was considered important to measure the sound power transfer function and the

surface-averaged mobility of a compressor primed for operation to obtain an accurate result for radiation efficiency.

Maidanik created a model for radiation efficiency of a thin, simply-supported, baffled plate, to which many analytical models have been compared [16]. To compare this model to a real-world application of structural acoustics involving a shell, Maidanik's plate radiation efficiency was calculated for a plate with all the same elastic and inertial properties as the shell encasing the compressor. The physical dimensions of this hypothetical plate were estimated by "unwrapping" the shell and treating it as a simply-supported plate.

Szechenyi, on the other hand, derived a thin, simply-supported, baffled cylindrical shell radiation efficiency model [17], which was compared to the measured radiation efficiency of the mass-loaded compressor unit shell. This model contains two parts: the first part with a frequency domain ranging from low frequencies to the shell's ring frequency, and the second part with a frequency domain ranging from the ring frequency to just above the critical frequency. Because the model is optimized for applications where the ring frequency is lower than the critical frequency, which is not true in this case, only the part accounting for a peak at the critical frequency is plotted.

## 2.8 Radiation Loss Factor

The *radiation loss factor*  $\eta_{rad}$  represents the portion of energy that is lost from a vibrating surface due to radiated sound. This loss factor is useful in statistical energy analysis, a method of monitoring the energy transmitted through a system of structures and cavities. The radiation loss factor follows the same behavior as the radiation efficiency, according to [14]

$$\eta_{rad} = \frac{\rho_0}{\rho_s} \frac{1}{k_0 h} \sigma \quad ; \quad k_0 = \frac{\omega}{c_0}, \quad (2-25)$$

where  $k_0$  and  $c_0$  are the wavenumber and sound speed, respectively, in the surrounding fluid.

Thus, the highest radiation loss factors are located at or near the critical frequency.

## 2.9 Noise Monitoring

Another transfer function can be computed for the purposes of monitoring a sound source. Given the resources and environment required to obtain the radiated sound power level with a measurement of sound pressure, a manufacturer with this task would be more interested in an effective method that measures surface acceleration rather than sound pressure. By measuring the sound power transfer function with a testing setup and space that conform to a verified standard, as well as measuring the surface-averaged response of the source due to a force at a drive point, one can evaluate a transfer function of sound power due to surface acceleration

$$\frac{P_{rad}}{\langle |\bar{a}|^2 \rangle} = \frac{P_{rad}}{\bar{F}^2} \div \frac{\langle |\bar{a}|^2 \rangle}{\bar{F}^2}. \quad (2-26)$$

The second term in blue is the squared, surface-averaged acceleration; this term is like the surface-averaged mobility, except the response has units of acceleration. By dividing the sound power transfer function by the acceleration, the force units cancel out, leaving a “manufacturer’s transfer function” that will allow the user to easily and accurately report the radiated sound power with a simple measurement of the surface-averaged acceleration of the desired sound source in any environment.

To verify this method of obtaining a simple function for radiated sound power, given surface acceleration, the compressor unit seen in Figure 2-16 was operated and tested by the same procedure as the initial radiated sound power testing. Time history data was taken with the accelerometers used for surface mobility testing and the microphones used for the sound power transfer function testing. The sound power level was calculated firstly by the method from the ANSI/ISO standard, shown in Equation (2-5), and secondly by scaling the surface-averaged acceleration by the “manufacturer’s transfer function” from Equation (2-26).

# Chapter 3

## Results & Discussion

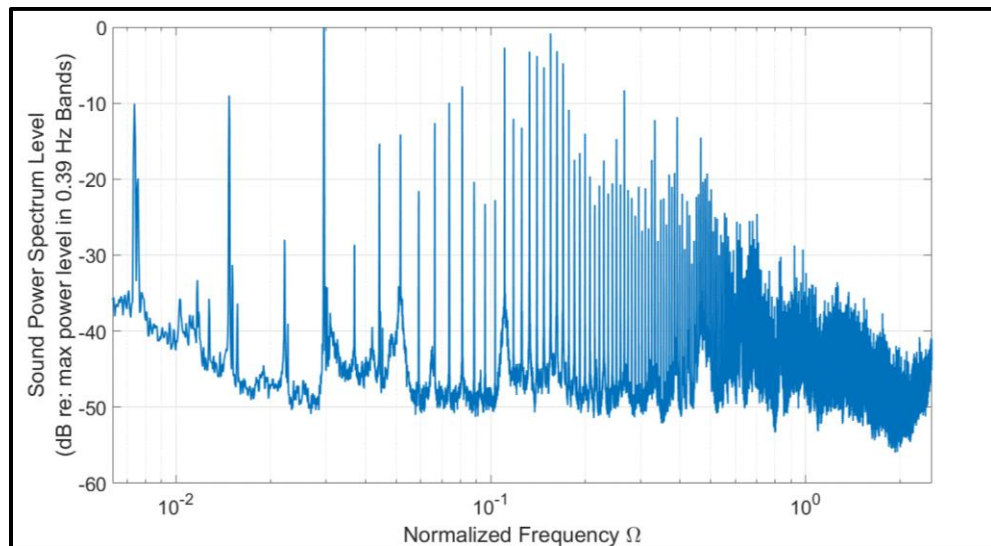
### 3.1 Identifying the Dominant Transmission Path

#### 3.1.1 *Radiated Sound Power*

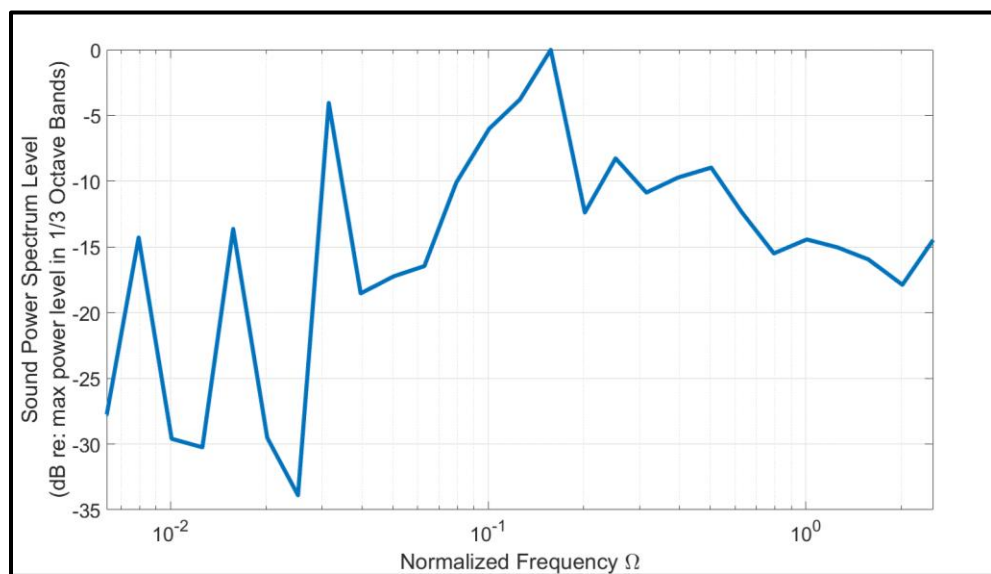
Figure 3-1a shows the narrow-band radiated sound power spectrum, subtracted by its maximum sound power spectrum level, of a compressor unit operating with an inlet temperature of 10 degrees Celsius and an outlet temperature of 46 degrees Celsius. The signal frequency is normalized by the shell's ring frequency for all results presented, including radiated sound power level; because there is no peak in magnitude at or beyond the ring frequency, future results are shown up to  $\Omega = 1$ . Narrow peaks in the spectrum are observed at the compressor's operating frequency and its harmonics, which remain visible roughly up to  $\Omega = 0.6$ . These tones have a significant influence on the sound power spectrum, as their magnitudes are 20 to 40 dB above the continuum. Because the harmonics, which have a small frequency separation, remain prominent at higher frequencies, it is likely that they coincide with structural or acoustic resonances, resulting in an increase in radiated sound power levels. This phenomenon appears to be the case, as some higher order harmonics have greater sound power level than those of lower order.

Figure 3-1b shows the sound power spectrum in one-third octave bands. The sound power spectrum is analyzed in one-third octave bands, because the human ear filters sound roughly in these bands. The shape of the spectrum proves unfavorable for human perception of sound. Figure 3-2 shows the A-weighting curve [18], often applied to unweighted levels, to demonstrate how people will perceive a noise source. Though there is considerable noise below

$\Omega = 0.1$ , the concern of the thesis does not lie there, particularly because people do not hear as well in that range as they do at higher frequencies. The curve shows that the human ear is most sensitive within frequencies between roughly  $\Omega \sim 0.1$  and  $\Omega \sim 0.6$ . Unfortunately, the high density of observable harmonics at mid-high frequencies increases the overall sound power within this frequency range, raising concern for sound perception.



(a)



(b)

**Figure 3-1. Normalized radiated sound power spectrum of the design of record compressor unit in (a) narrow bands and (b) in one third octave bands.**

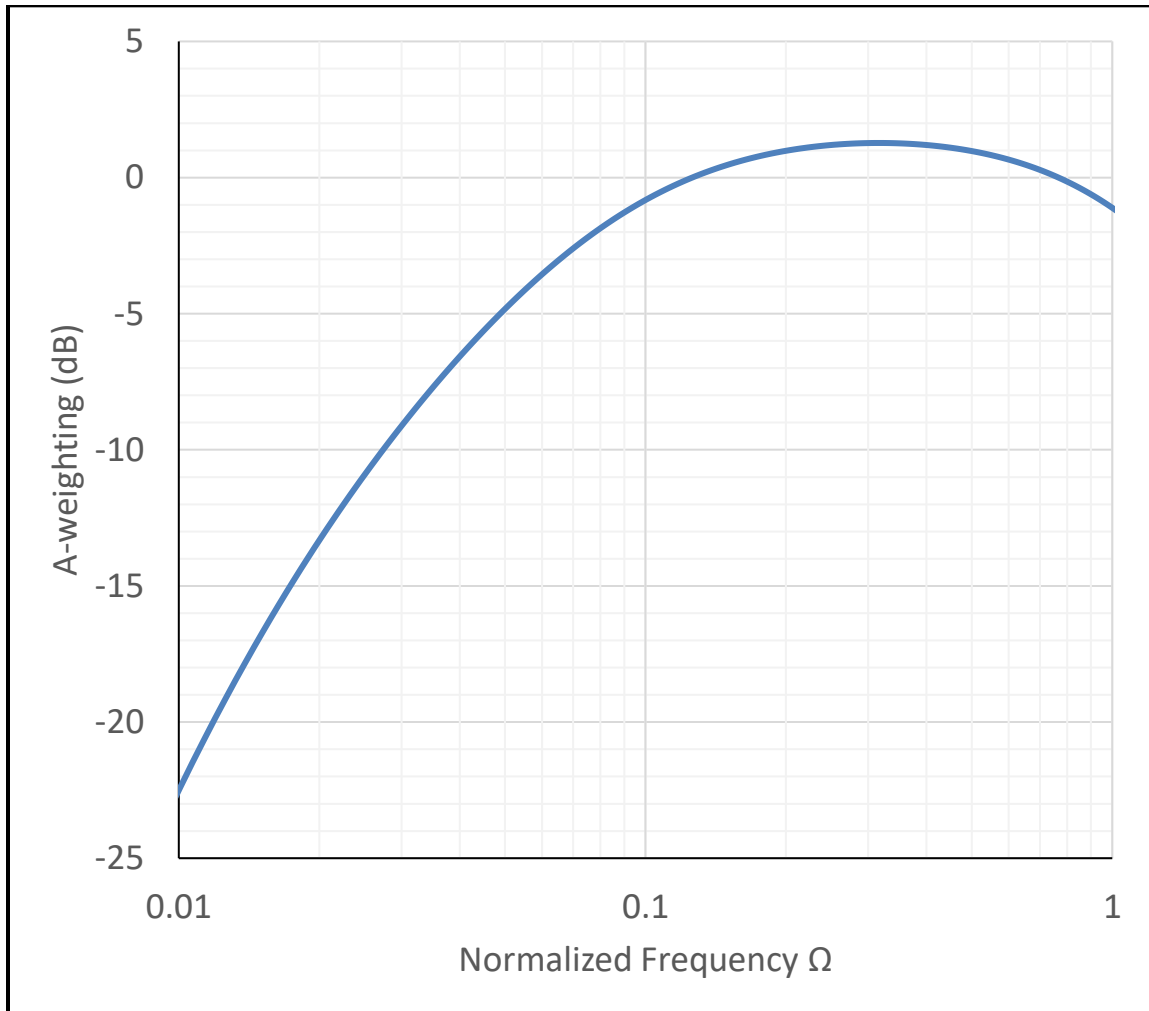
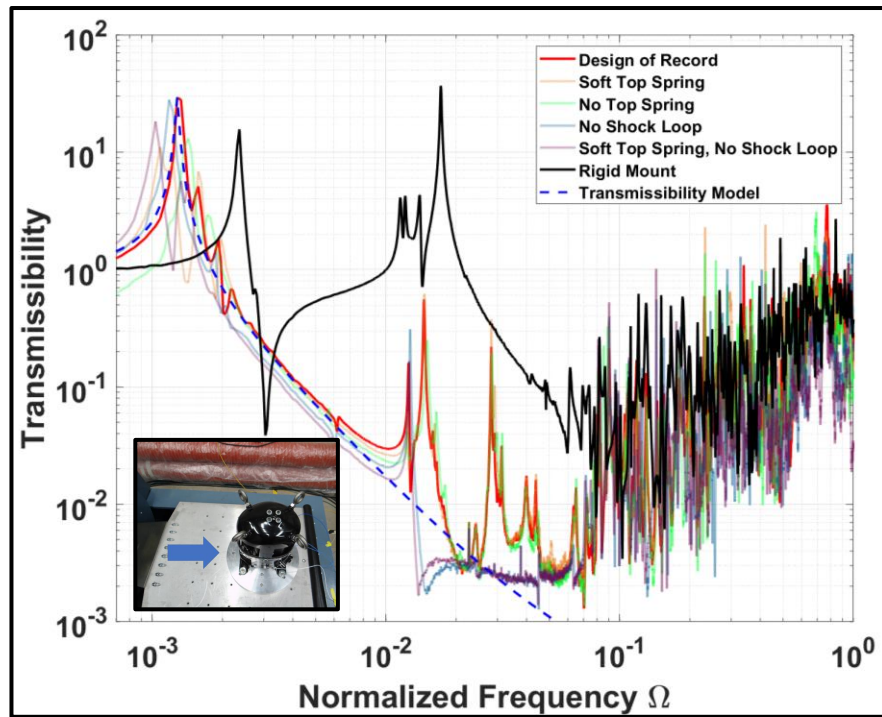


***Figure 3-2. A-weighting curve, commonly applied to sound power levels to give an accurate representation of how people perceive sound sources below 100 dB (unweighted).***

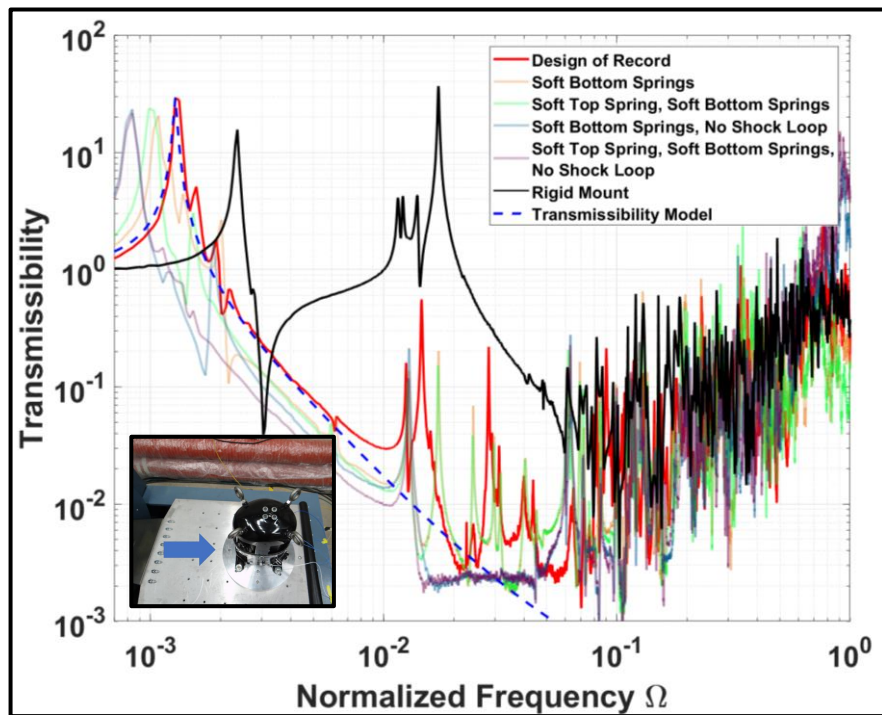
### 3.1.2 *Transmissibility*

The graphs in Figures 3-3 through 3-5 depict the transmissibility measured from the enclosure at one mounting bracket to its corresponding side of the compressor crankcase. The solid red line in each graph shows the transmissibility of the design of record configuration. The transparent colored lines represent other configurations of the mounting (bottom) springs, the stabilizer (top) spring, and the shock loop. Alternate configurations with production-line mounting springs are shown in Figures 3-3a, 3-4a, and 3-5a; those with a softer set of mounting springs are shown in Figures 3-3b, 3-4b, and 3-5b. The black line shows the transmissibility of the rigidly mounted condition. The dashed line is the calculated transmissibility model of a single degree-of-freedom system with the fundamental resonance frequency and damping ratio of the design of record case; the line was computed by solving Equation (2-8) for the damping ratio – given the fundamental resonance frequency and its corresponding transmissibility magnitude – of the design of record configuration in each direction. The orientations of the compressor on the shaker and the table are shown in the bottom left of each graph. Arrows indicate the directions in which the compressor was shaken and the transmissibility was measured.

The first major observation is that the transmissibility for each vibration-isolated case does not behave like a characteristic single degree-of-freedom system. Due to the rocking motion of the mass, there are coupled modes that exist just after the fundamental resonance. More importantly, however, the transmissibility steadily increases with frequency as  $\Omega > 0.06$ . Many sharp peaks are found within this range, and the behavior is generally consistent across all vibration isolation configurations.

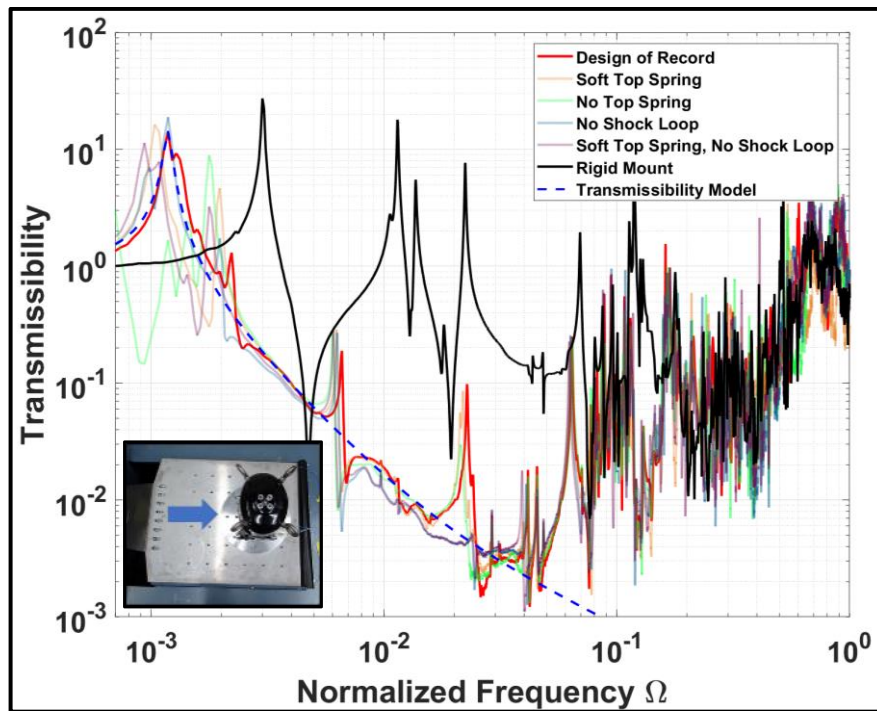


(a)

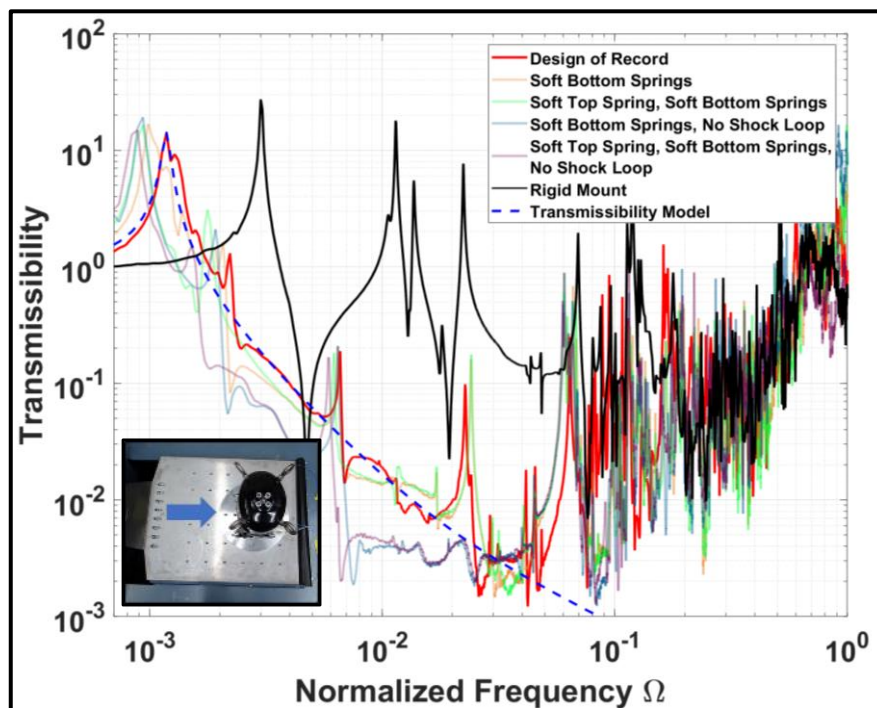


(b)

Figure 3-3. Transmissibility of inoperable unit from enclosure at mounting brackets to compressor crankcase, forced and measured in the X direction, as indicated by the arrow.

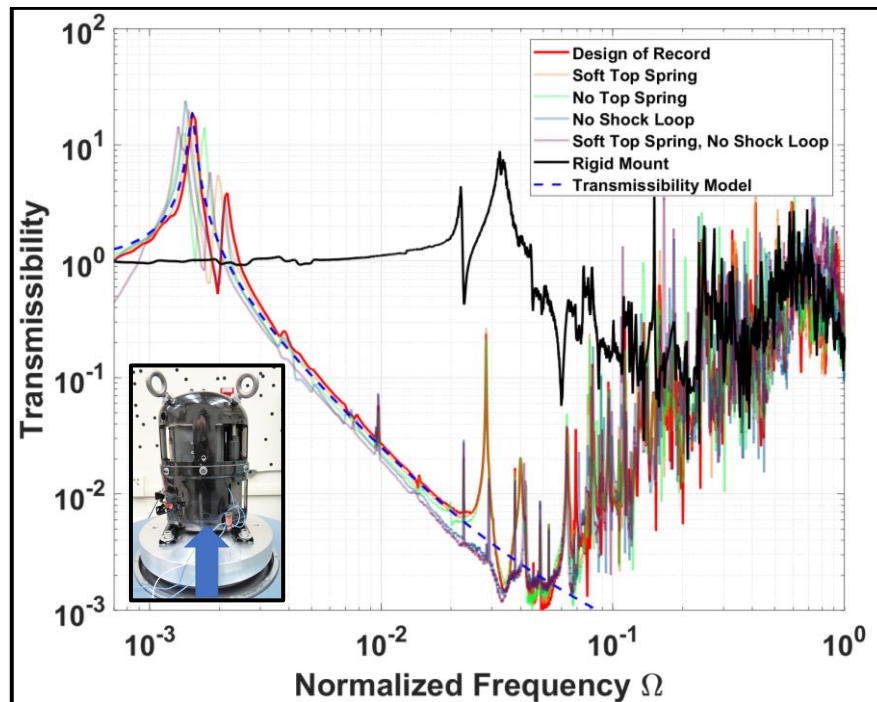


(a)

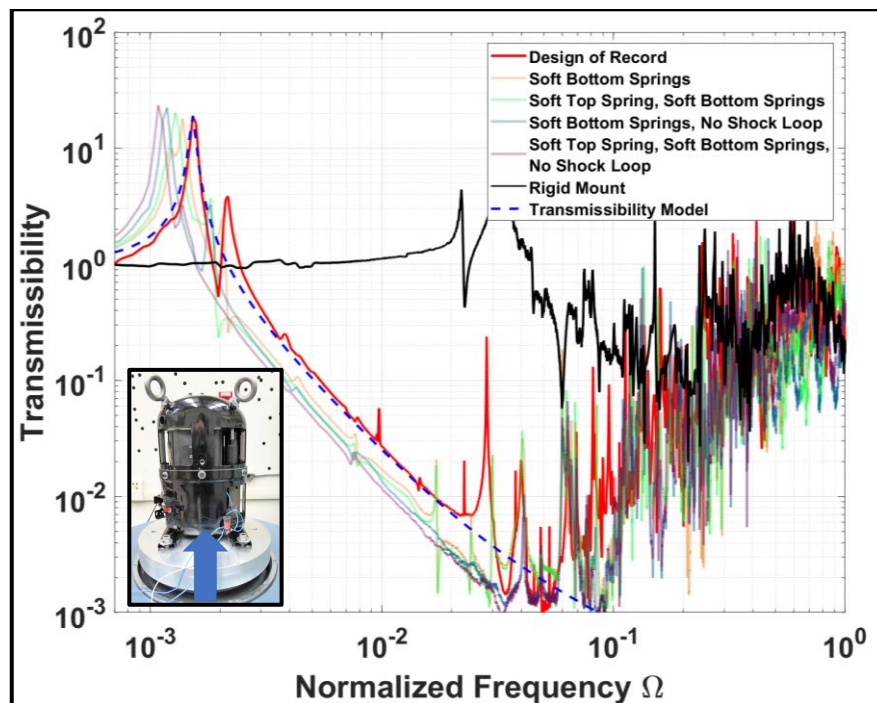


(b)

Figure 3-4. Transmissibility of inoperable unit from enclosure at mounting brackets to compressor crankcase, forced and measured in the Y direction, as indicated by the arrow.



(a)



(b)

Figure 3-5. Transmissibility of inoperable unit from enclosure at mounting brackets to compressor crankcase, forced and measured in the Z direction, as indicated by the arrow.

The other significant observation is that the transmissibility of the rigidly mounted compressor, though equal to 1 in the Z-direction (Fig. 3-5) at low frequencies, converges with that of each vibration-isolated case as the frequency increases. Even when the compressor is hard bolted to the mounting bracket, which is welded and pressed onto the shell, there are resonances and antiresonances present in the middle of the frequency spectrum, which may be contributed to compliant characteristics of the shell in the X and Y directions. Still, the high-frequency behavior of the rigidly-mounted assembly remains relatively the same as that of all the other configurations. This phenomenon provides a fair argument to suggest that the properties of the enclosure affect the transmissibility of any type of mount and, therefore, evaluating the structural characteristics of the operable compressor enclosure can prove useful to solving the noise control problem.

The shock loop, which provides additional rocking stability to the compressor and allows pressurized refrigerant to be discharged from an operating unit, has an impact on the transmissibility of the system. Though minor in the evaluation of overall transmissibility for these cases, the transmissibility measurement corresponding to the absence of the shock loop shows notable differences from its inclusion in the assembly. A few large peaks found within  $0.01 < \Omega < 0.05$ , present in cases with the shock loop, are removed along with the component itself. Finite element modeling of the shock loop fixed on the bottom (Figure 3-6) shows a few modes with frequencies that correlate well with those of the unique peaks in the transmissibility of shock loop inclusive configurations. These findings suggest that the shock loop has structural resonances that play a key role in transmitting vibrations directly to the enclosure, thereby bypassing the springs mounted on top and bottom. Again, the high-frequency behavior was constant across all vibration isolated cases, whether the shock loop was present or not. Still, it is presumed that the shock loop will become of concern during the process of designing a practical noise control option.

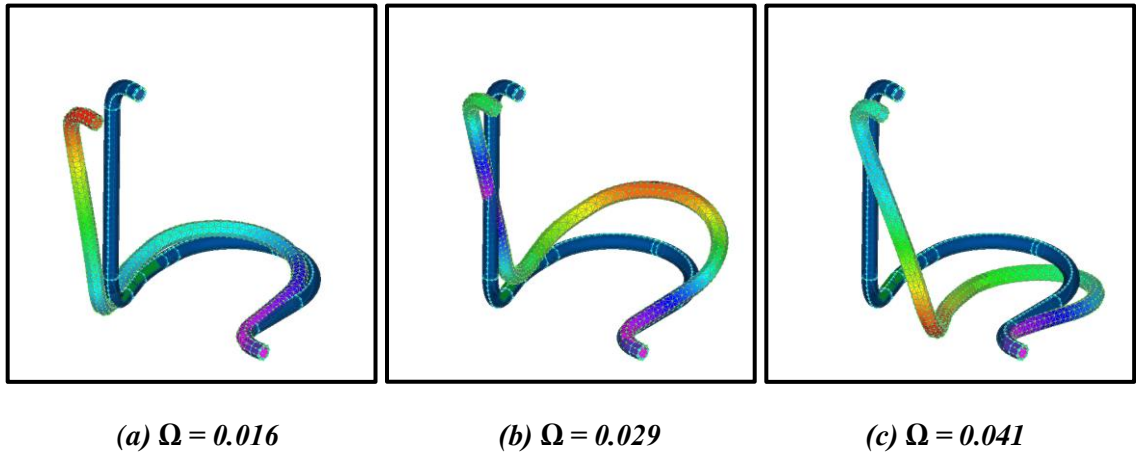


*Figure 3-6. Shock loop modes computed with finite element analysis. Peaks in the transmissibility of compressor assembly configurations with the shock loop installed correlate well with resonance frequencies of these modes.*

### 3.1.3 Comparing Radiated Sound Power and Transmissibility Levels

The transmissibility testing has led to the possibility of a correlation between radiated sound power level and transmissibility between the hermetic compressor and its housing. The radiated sound power of the design of record unit was subtracted from that of the rigidly mounted unit, both measured by Bristol. Then, the transmissibility of both the windowed units – rigidly mounted and design of record – was averaged along all three directions, and the latter was subtracted from the former. Figure 3-7 compares the trends in these differences in 1/3-octave bands. As  $\Omega > 0.06$ , in the same range that the transmissibility curves converge, the radiated sound power difference falls close to zero. It is clear from this comparison that throughout most of the frequency spectrum, particularly in regions where human hearing is the most sensitive, the radiated sound power goes roughly as the transmissibility between the compressor and its enclosure. Therefore, it is determined that the mechanical transmission path is the primary obstacle for noise control.

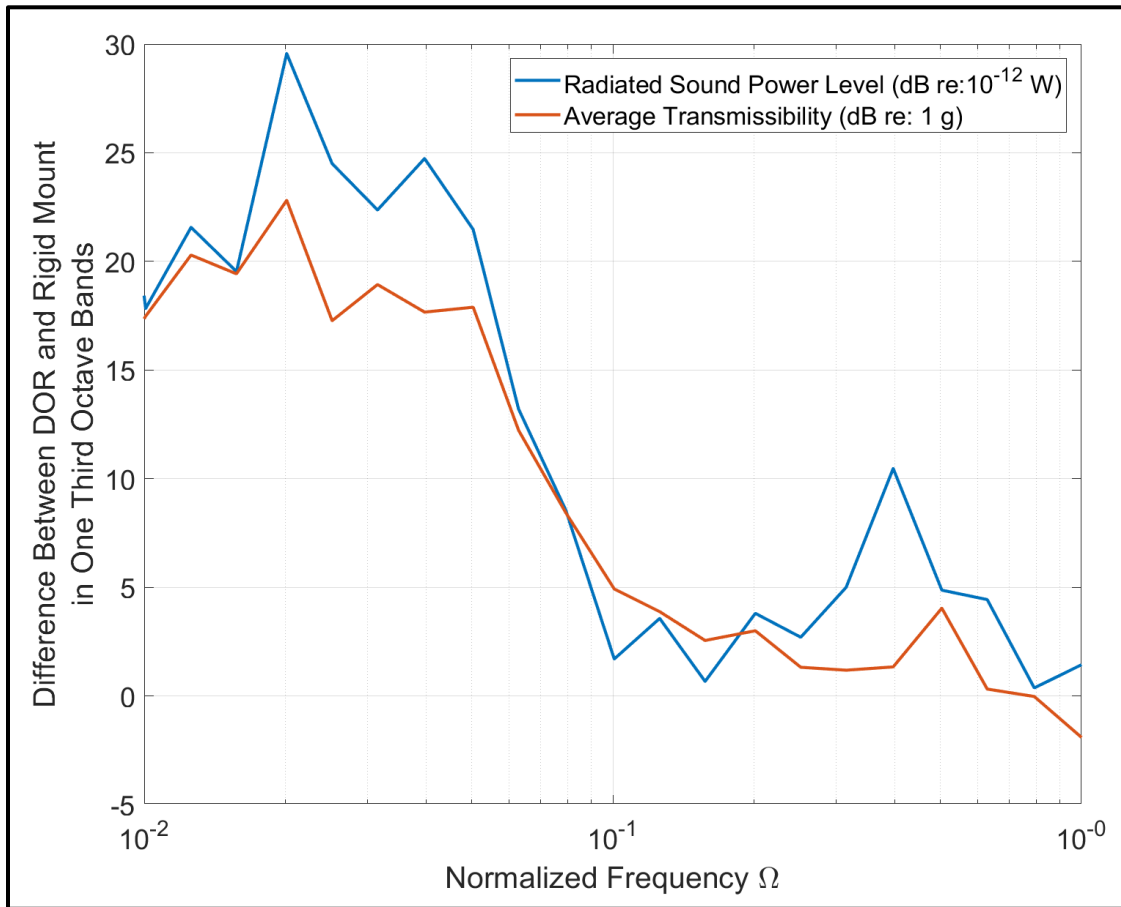


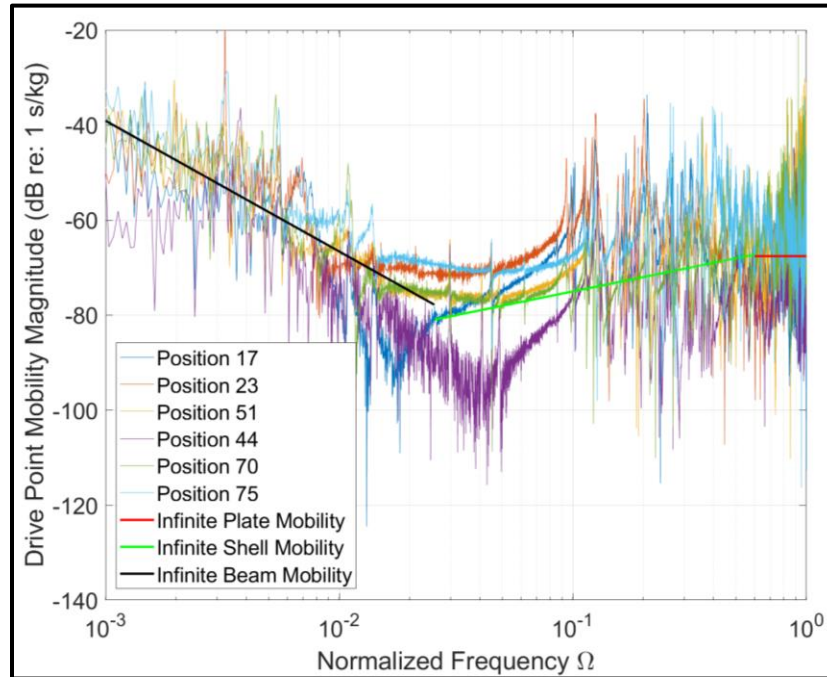
**Figure 3-7. Radiated sound power level (blue line) and transmissibility level (orange line) of rigidly mounted compressor minus those of the design of record unit, both in dB. Reference values are given in the legend.**

## 3.2 Characterizing the Shell Structure

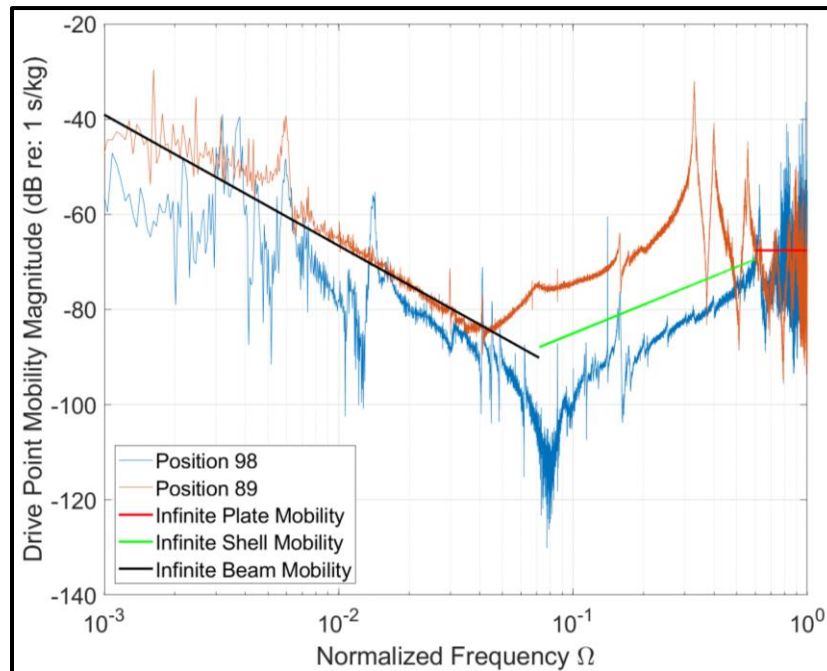
### 3.2.1 Drive Point Mobility

Figure 3-8 shows the drive point mobilities of the operable, design of record compressor. These mobilities are compared to the predicted infinite beam, shell, and plate behaviors [13] – which were calculated by Equation (2-20) and are shown in black, green, and red, respectively – in order to determine the structural behavior of the enclosure at different frequency ranges. The drive point mobilities are split up into two groups; the first six positions were measured on the elliptical cylindrical portion of the enclosure, while the last two were measured on top of the upper housing, or along the “domal” portion of the enclosure (see Figure 2-14). On the cylindrical enclosure, the presence of shell mode activity spans a wide range of frequencies ( $0.02 < \Omega < 0.6$ ), including the most sensitive range of human hearing and the frequencies with high radiated sound power levels. On the domal enclosure, the shell modal activity cut on depends much more heavily on the measurement location. For position 98, where there is relatively more curvature, shell modes do not cut on until  $\Omega \sim 0.07$ . Still, this cut on allows shell modal activity within the frequency range of interest. It is determined from these measurements that structural cylindrical shell modes should receive special attention, as the properties of the enclosure that make the current design of the mounting arrangement problematic for noise control are analyzed.

It is noted that the accelerometers used for these measurements were placed in positions with a variety of structural features in order to evaluate how the low-frequency cut-on of shell modes would change compared to that of a cylindrical shell with a uniform radius and thickness. For example, position 44 is on the lap weld joint between the upper and lower housings, where the thickness is doubled. Because the cut-on frequency of shell modes is directly proportional to the thickness of the shell, the actual low-frequency cut-on is approximately twice



(a)



(b)

**Figure 3-8. Drive point mobility of eight measurement points on the compressor shell, as labeled in Figure 2-13, compared to trends of infinite plate, shell, and beam mobility as formulated by Cremer, Heckl, & Ungar. Measurement points were split into those on the cylindrical portion (a) and those on the domal portion (b) of the enclosure, showing the influence of curvature on the low-frequency cut-on of shell mobility.**

that of the predicted cut-on. Furthermore, the curvature of the domal portion of the enclosure is greater away from the top spring mount than closer to it; therefore, as position 89 is centered at the top spring mount and position 98 is further away, the cut-on of shell modes is lower in frequency for position 89 than position 98. This phenomenon happens because the radius of a cylinder of uniform curvature is greater for position 89 than position 98, and the cut-on frequency is inversely proportional to the radius of the cylinder. In order to account for the higher curvature of the top portion of the shell, the radius used for the model in Figure 3-8b is less than that used for the model in Figure 3-8a; as a result, the shell cut-on frequency is raised. Because the infinite shell mobility cut-on is keen to shift with subtle changes in the structural properties of the enclosure, careful skepticism is placed on the absolute applicability of the predicted model to case studies such as this one, though the model serves as a helpful guide.

At some drive points, the mobility is very low for some frequencies within  $0.4 < \Omega < 0.8$ . It is likely that movement of the enclosure is highly impeded at the locations of the drive points when excited at these frequencies. Because mobility is sharply reduced rather than increased, it is expressed that this phenomenon occurs at the antiresonances of the structure.

### ***3.2.2 Modal Analysis and Surface-Averaged Mount Mobility***

Modal analysis was performed on a charged, operable compressor, and mode shapes were obtained to test the application of theoretical shell estimates. In Figure 3-9, the experimental modal frequencies are compared to documented estimates [13] of cylindrical shell modes with axial (m) and circumferential (n) mode orders, and the shapes of these modes are juxtaposed alongside each point. Although the  $n = 0, 1$  mode orders are not identifiable in the experimental results, the modes from  $n = 2$  to  $n = 7$  are found to be comparable to the predicted modes. The cylinder is not perfectly uniform along its height, with some surfaces contracting inward;

therefore, the predictions slightly underestimate the resonance frequencies of each mode. Still, the Cremer model proves useful for estimating cylindrical shell modal frequencies.

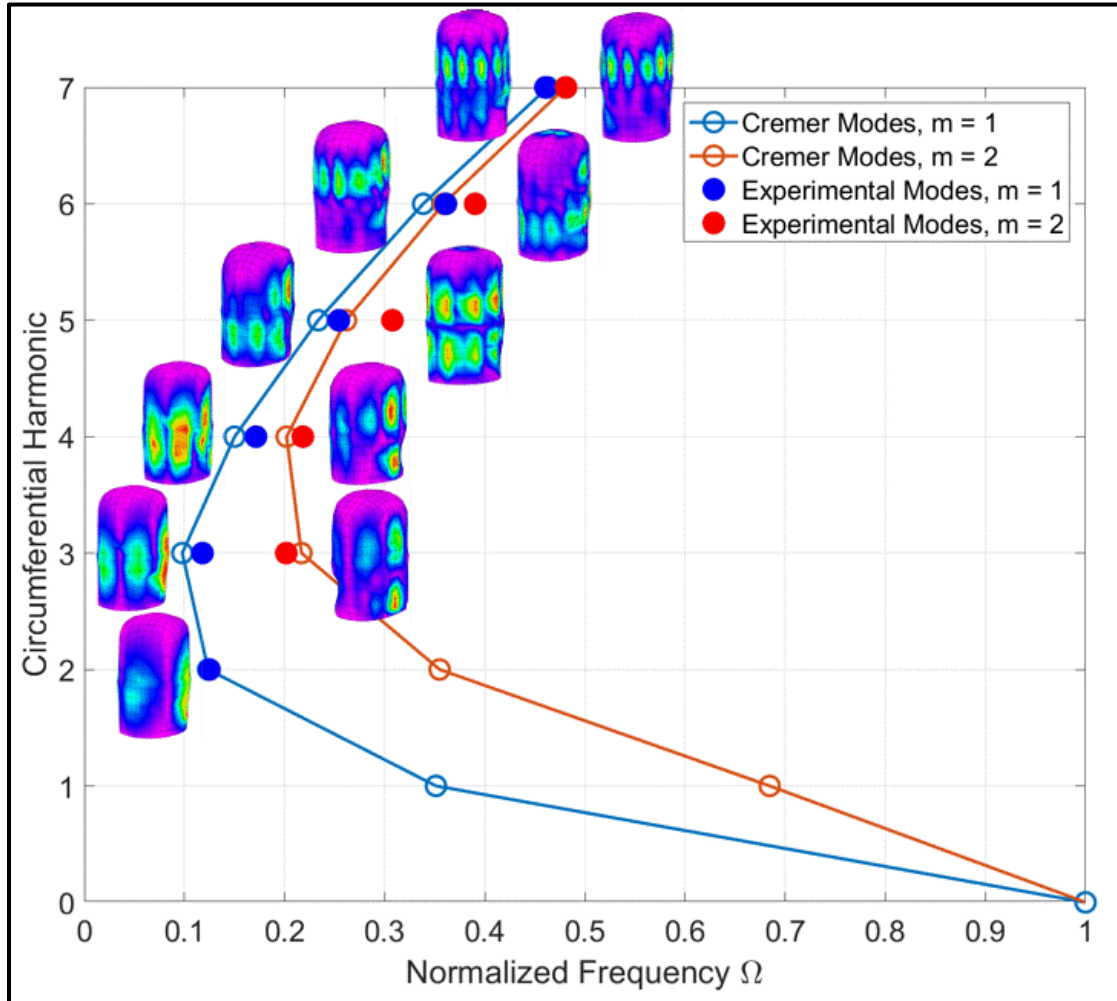
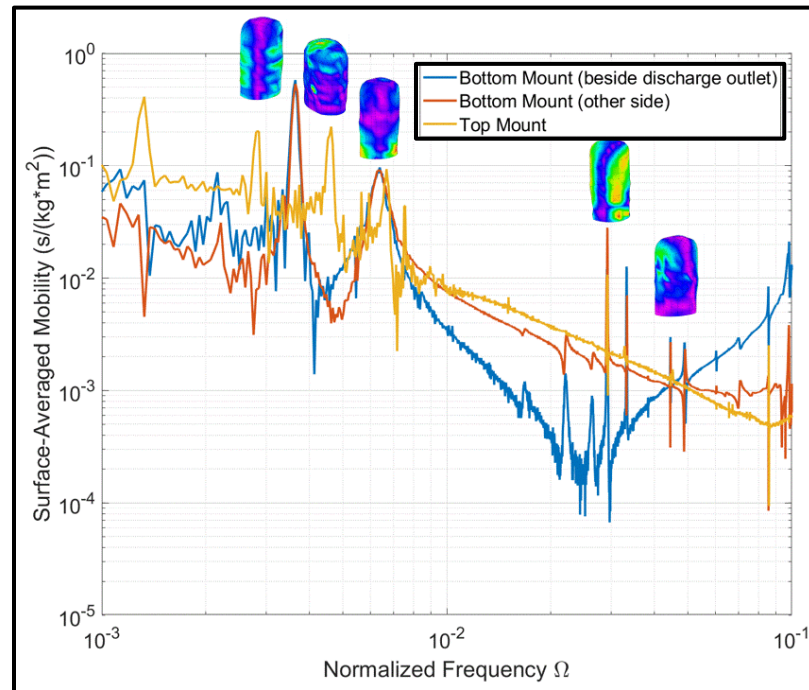


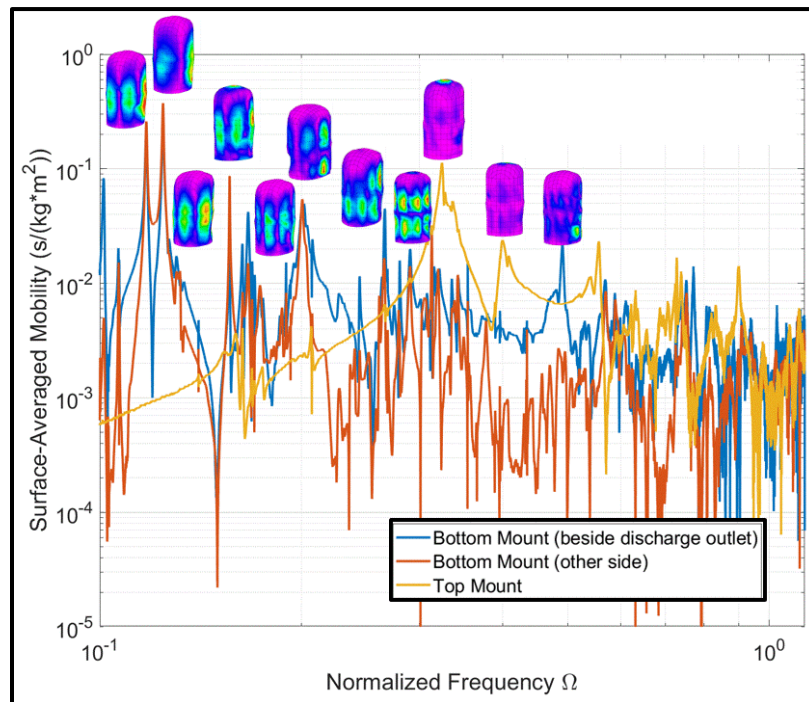
*Figure 3-9. Cremer cylindrical shell modal estimates compared to shell modes found through modal analysis.*

In addition to comparing experimental modal frequencies with those predicted by a theoretical model, the surface-averaged mobility of each spring mount on the shell was calculated to find modes stimulated by the mounts. Mode shapes found in the modal analysis are displayed by their corresponding peaks in mobility in Figure 3-10. The first graph of the surface-averaged mobility and the mode shapes reveals that the bottom mounts excite a few beam modes below  $\Omega$

= 0.06, and that the top mount excites a beam mode at  $\Omega = 0.0045$ . The second graph shows a plethora of identifiable cylindrical shell modes within the frequency range of interest ( $0.1 < \Omega < 0.6$ ) that are activated by the bottom and top mounts. These findings confirm the presence of low-frequency beam modes and mid to high-frequency shell modes, as indicated by the drive-point mobility curves. More importantly, however, the mode shapes just above  $\Omega = 0.1$  show high mobility at the locations of the bottom and top mounts. It is then resolved that, during operation, a compressor mounted by its current vibration isolation configuration will excite the surrounding structure at the antinodal regions of many modes. The high mobility at these shell modes also means that the foundation, on which the compressor is mounted, is not sufficiently rigid for any vibration isolation system to be effective. Therefore, it is necessary to redesign the suspension system in such a way as to mount the compressor onto a more rigid foundation, away from high-mobility surfaces.



(a)



(b)

**Figure 3-10. Surface-averaged mobility at mount locations with mode shapes compared to selected peaks. Two frequency ranges are displayed separately to show presence of beam modes (a) and cylindrical shell modes (b). The blue line is measured at position 17, the orange line is measured at position 23, and the yellow line is measured at position 89 (see Figure 2-13).**

### 3.2.3 Loss Factor

Figure 3-11 shows the loss factors calculated for all the modes found in the modal analysis. The shell modes identified in Figure 3-10b are highlighted with their mode shapes. In addition, the critical frequency, at which structural and acoustic waves travel at the same speed, is indicated. The loss factors remain small at low frequencies and increase with frequency up to  $\Omega \sim 0.3$ ; then, the loss factors converge to a nominal value with increasing frequency. It is worth noting that some modes have a loss factor close to 10 times greater than others. This phenomenon might be the case because of a significant contribution of radiation loss to the system. The behavior of the structural losses is similar to that of radiation efficiency, which converges to a value of 1 above the critical frequency and is presented later in this chapter.

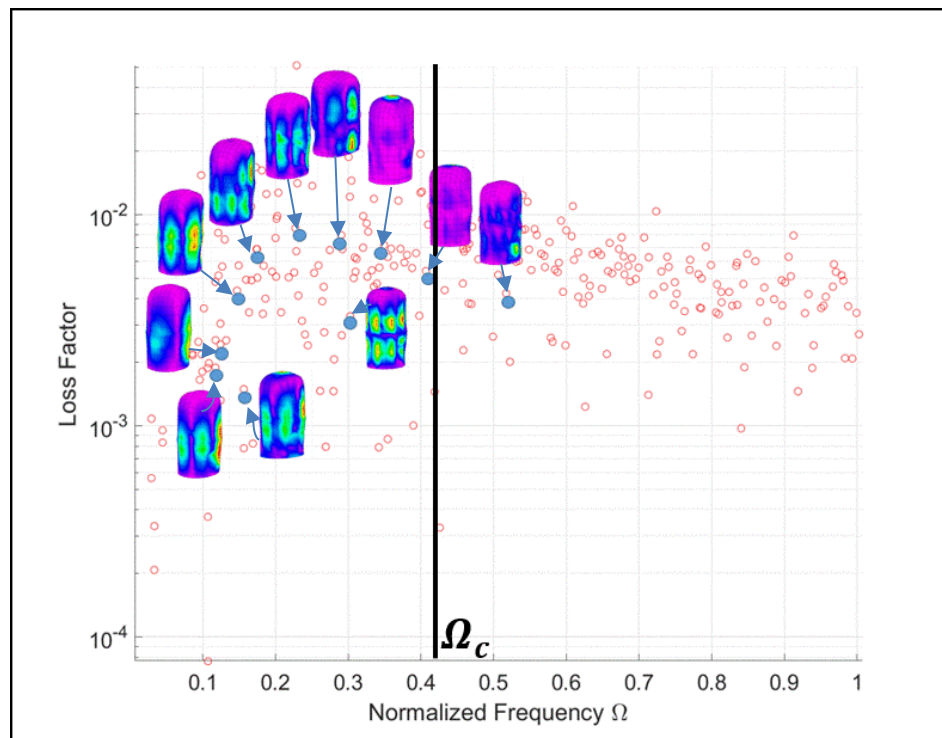
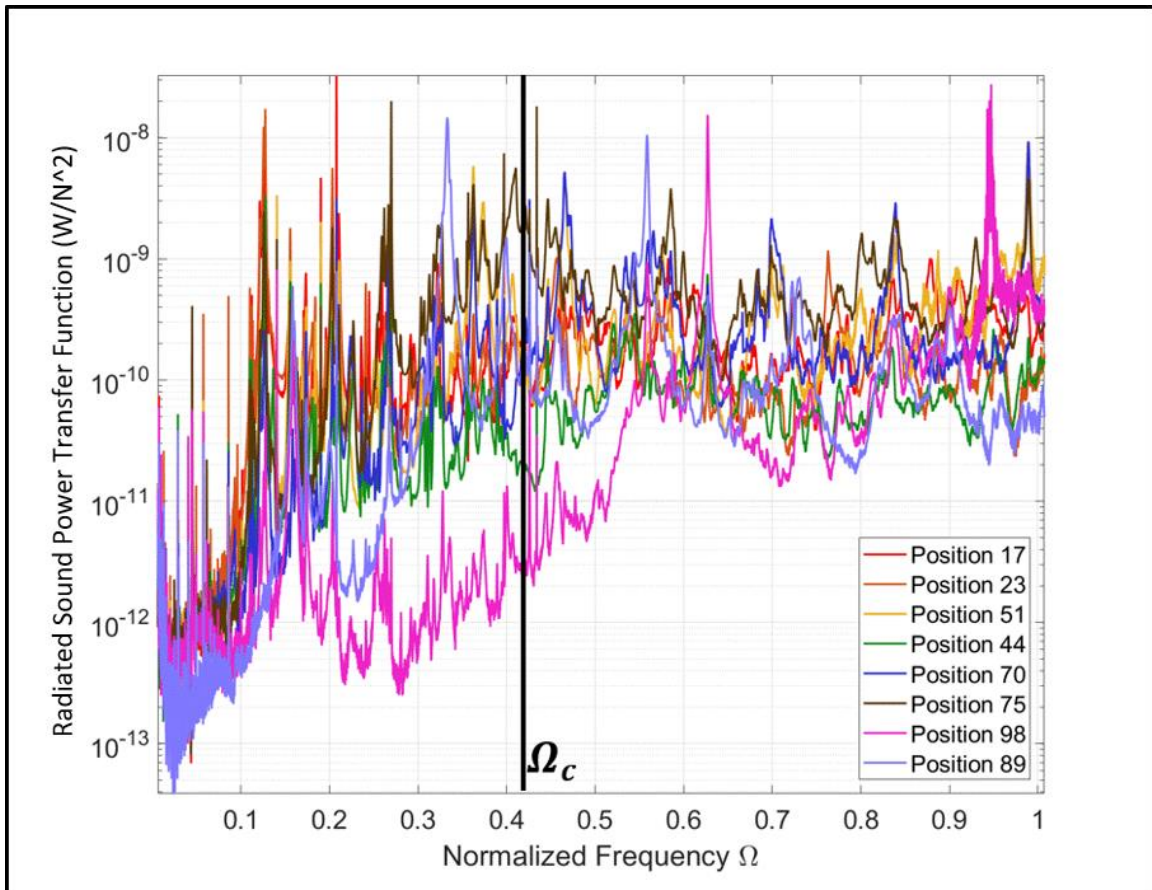


**Figure 3-11.** Loss factors calculated from modal analysis. The loss factors of the significant modes displayed in Figure 3-6 are identified with blue markers, and their mode shapes are placed beside them. The normalized critical (coincidence) frequency  $\Omega_c = 0.418$  is identified with a vertical black line.

### 3.3 Effects of the Shell Structure on the Radiated Sound

#### 3.3.1 *Sound Power Transfer Function*

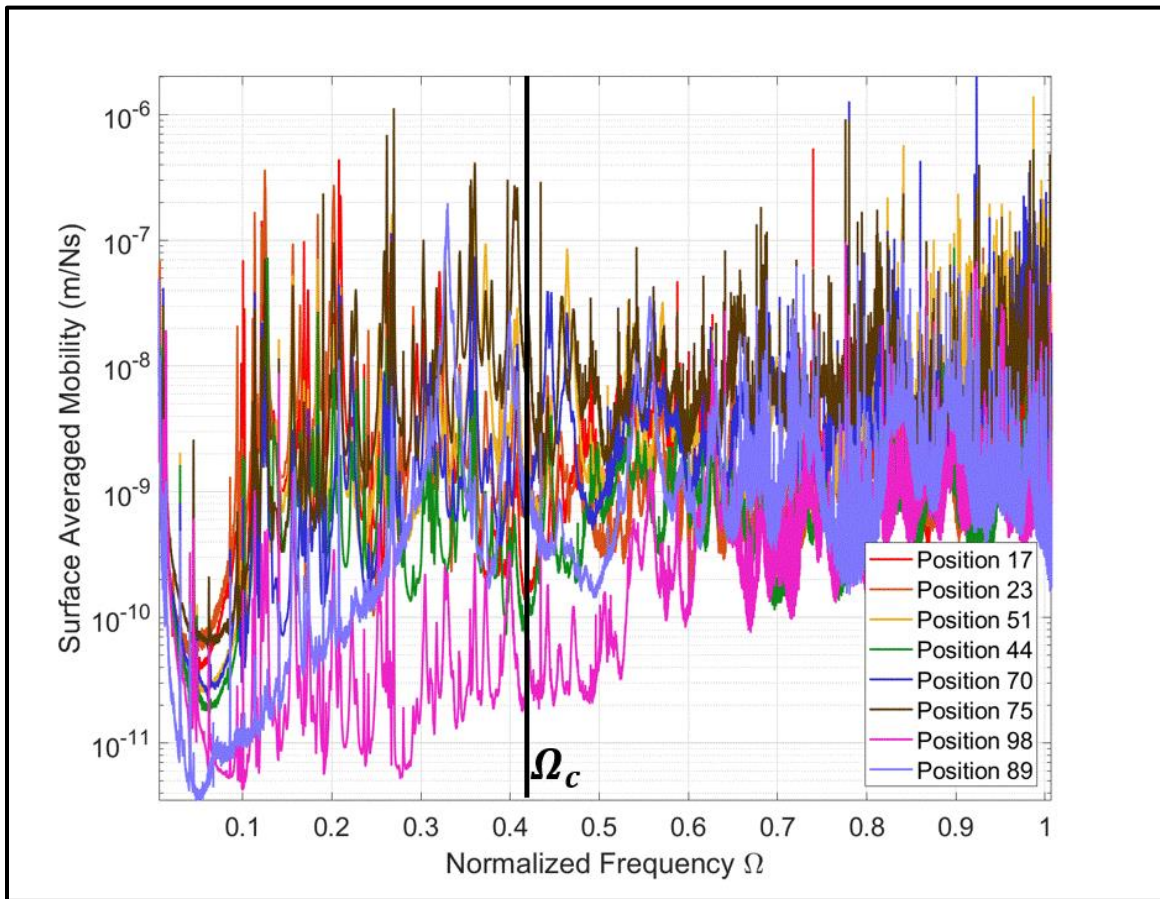
Figure 3-12 shows the sound power transfer functions for the eight drive points pictured in Figure 2-14. It is evident by the functions that the enclosure has a significant level of influence on the radiation of sound within the frequency range of interest. The normalized critical frequency  $\Omega_c$ , labeled with a black vertical line, has been defined as the frequency at which structural and acoustic waves travel at the same speed. Near this frequency, sound radiates well; it is, therefore, unfortunate that the critical frequency not only sits comfortably within the most sensitive range of human hearing, but that it also thrives in close proximity with peaks in the transfer functions. It should be noted that the critical frequency appears lower than the estimate indicated in the figure; this indication is likely due to the internal pressurization of the compressor unit, stiffening the shell and shifting the actual critical frequency lower, approximately at  $\Omega = 0.3$ .



*Figure 3-12. Sound power transfer function computed from each accelerometer position. The normalized critical (coincidence) frequency  $\Omega_c = 0.418$  is identified with a vertical black line.*

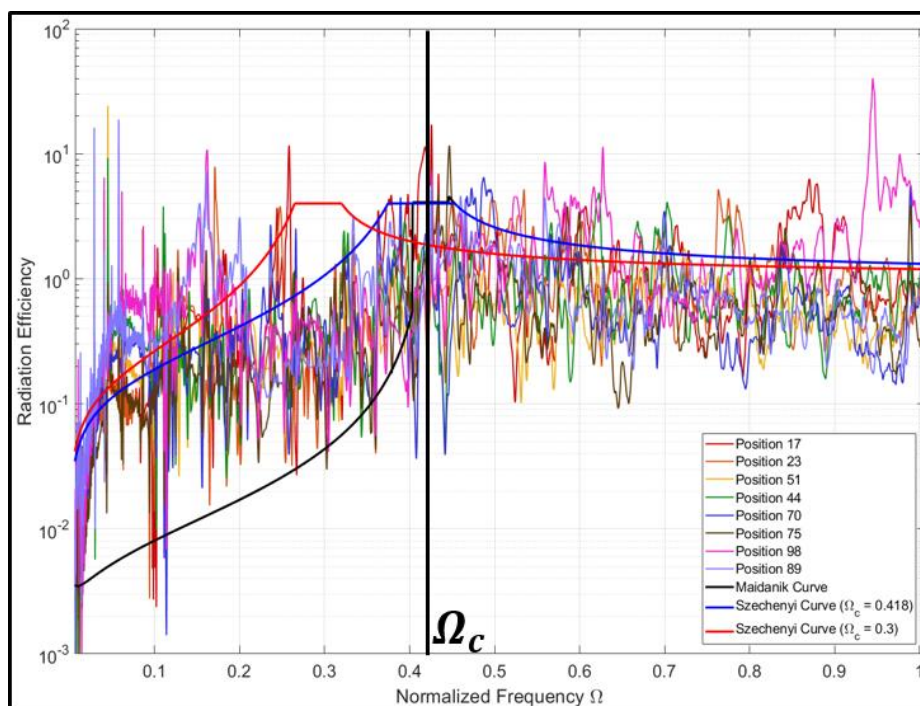
### 3.3.2 Radiation Efficiency

Figure 3-13 shows the surface-averaged mobility of the entire surface due to forces at each of the positions listed in the legend (see Figure 2-14). The normalized critical frequency is labeled in the figure to show its location along the spectrum.

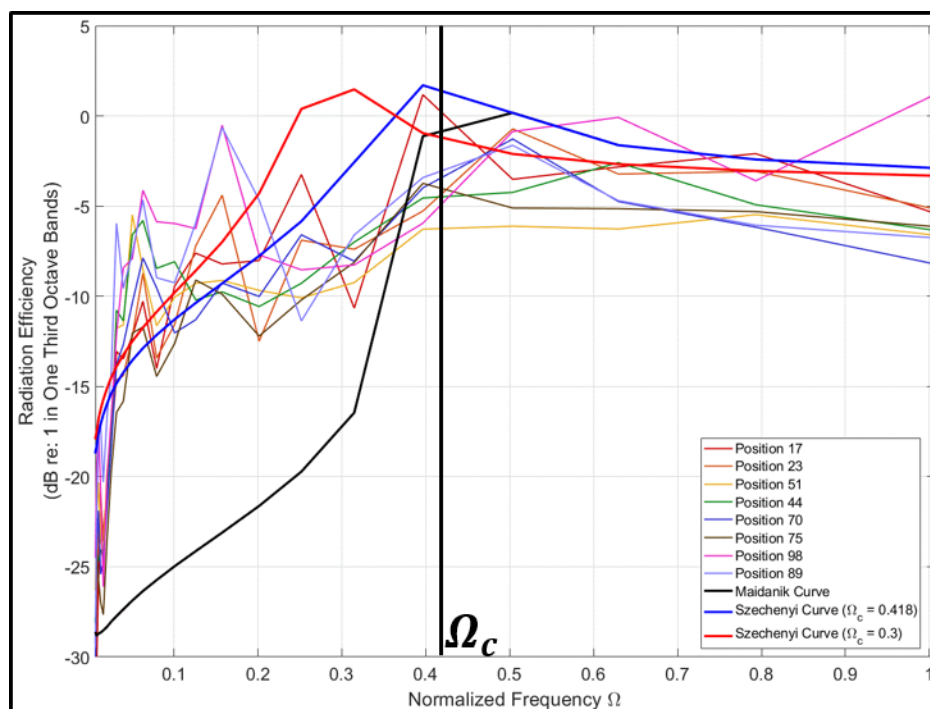


**Figure 3-13.** *Surface-averaged mobility of the entire shell measured at each accelerometer position. The normalized critical (coincidence) frequency  $\Omega_c = 0.418$  is identified with a vertical black line.*

Figure 3-14 shows the radiation efficiency at each accelerometer location, calculated using the sound power transfer functions, the surface-averaged mobility, and the fluid impedance of the air surrounding the compressor. Again, the normalized critical frequency is labeled in the figure to show its location along the spectrum. While some of the shell modes previously analyzed are found below the critical frequency, they still radiate well enough to significantly contribute to the noise spectrum of the compressor.



(a)



(b)

**Figure 3-14. Radiation efficiency measured at each accelerometer position, compared with the calculated Maidanik and Szechenyi curves, in (a) narrow bands and (b) one third octave bands. The normalized critical frequency  $\Omega_c = 0.418$  is identified with a vertical black line.**

The Maidanik radiation efficiency curve, discussed in Section 2.7 and shown in black in Figure 3-14, was also computed and compared to the experimental radiation efficiency. While the Maidanik curve is well suited for prediction of radiation efficiency trends at and above the critical frequency, it misses the mark below the critical frequency. The model, assuming a thin, simply-supported, baffled plate, underestimates the influence of several shell modes, which are prominent between  $\Omega = 0.025$  and  $\Omega = 0.6$ ; therefore, the Maidanik model does not prove to be a reliable estimation of radiation efficiency for this application.

The Szechenyi radiation efficiency model, discussed in Section 2.7 and shown in blue for  $\Omega_c = 0.418$ , fits the measured curves better. While the Maidanik curve models radiation efficiency at and above the critical frequency well, the Szechenyi model more accurately predicts the entire trend in radiation efficiency, including that which is below the critical frequency, because it accounts for the coupling that occurs with membrane waves, which move faster than bending waves. Above the critical frequency, the  $\Omega_c = 0.418$  case falls on top of the Maidanik curve. The major fault in the Szechenyi model is that it predicts a much greater peak at the critical frequency than measured; therefore, the radiation efficiency near that frequency is limited to approximately match the Maidanik curve. Because of how well it aligns with the measured radiation efficiency at nearly all frequencies, it is determined that the radiation efficiency of a cylindrical shell is more accurately estimated with the Szechenyi curve than the Maidanik curve.

In Figure 3-14, the cylindrical shell model (Szechenyi) is plotted with both the predicted normalized critical frequency of 0.3 in red and the calculated, estimated value of 0.418 in blue. Though the sound power transfer functions suggest the former value for the critical frequency, the radiation efficiency models that use the latter value fit the measured functions better. It is unclear why the models that neglect shell thickness and mass loading predict the radiation efficiency better than those that take those factors into account.

### ***3.3.3 Noise Monitoring***

As mentioned previously, a noise monitoring function of radiated sound power per surface-averaged acceleration can be used in conjunction with surface acceleration measurements to accurately measure the sound power radiated from any sound source. Figure 3-15 shows this particular function calculated at each of the eight accelerometer positions. Figures 3-16 and 3-17 show the maximum normalized radiated sound power level, computed using the averages of the noise monitoring function and the surface-averaged acceleration, as well as the radiated sound power measured with the ANSI/ISO 3745:2012 standard. The accelerometer-based method generally reports a sound power level within +/- 5 dB of the standard measurement, with a few exceptions of inaccuracies in the peak magnitudes at the harmonics of the compressor's operating frequency. This uncertainty is attributed to measurement uncertainty, as there was hardware in place for acquiring data that may have influenced the results of the test. Nevertheless, the accelerometer-based method follows the same trend as the ANSI/ISO standard and in fact reports similar values in dB at higher frequencies, especially those within the most sensitive range of human hearing. Knowing that an operating compressor's sound power level can be monitored using surface-averaged vibration, one can use the monitoring function, obtained from a well-documented standard of measuring sound power level in a hemi-anechoic chamber, to solve for the radiated sound power level without the need for a multitude of microphones or a sophisticated acoustics laboratory. This method has the potential to facilitate sound power measurements for any noise source moving forward.

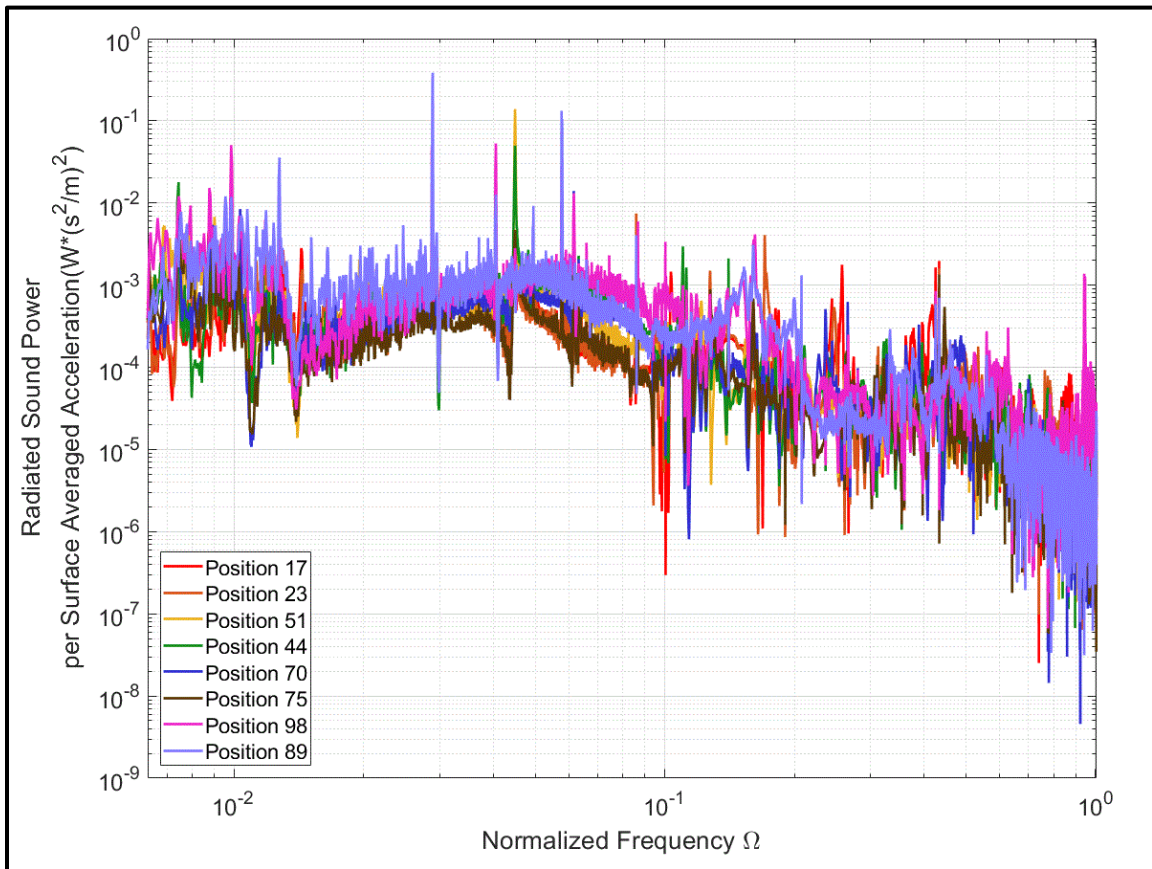


*Figure 3-15. Sound power per surface-averaged vibration calculated at each position.*

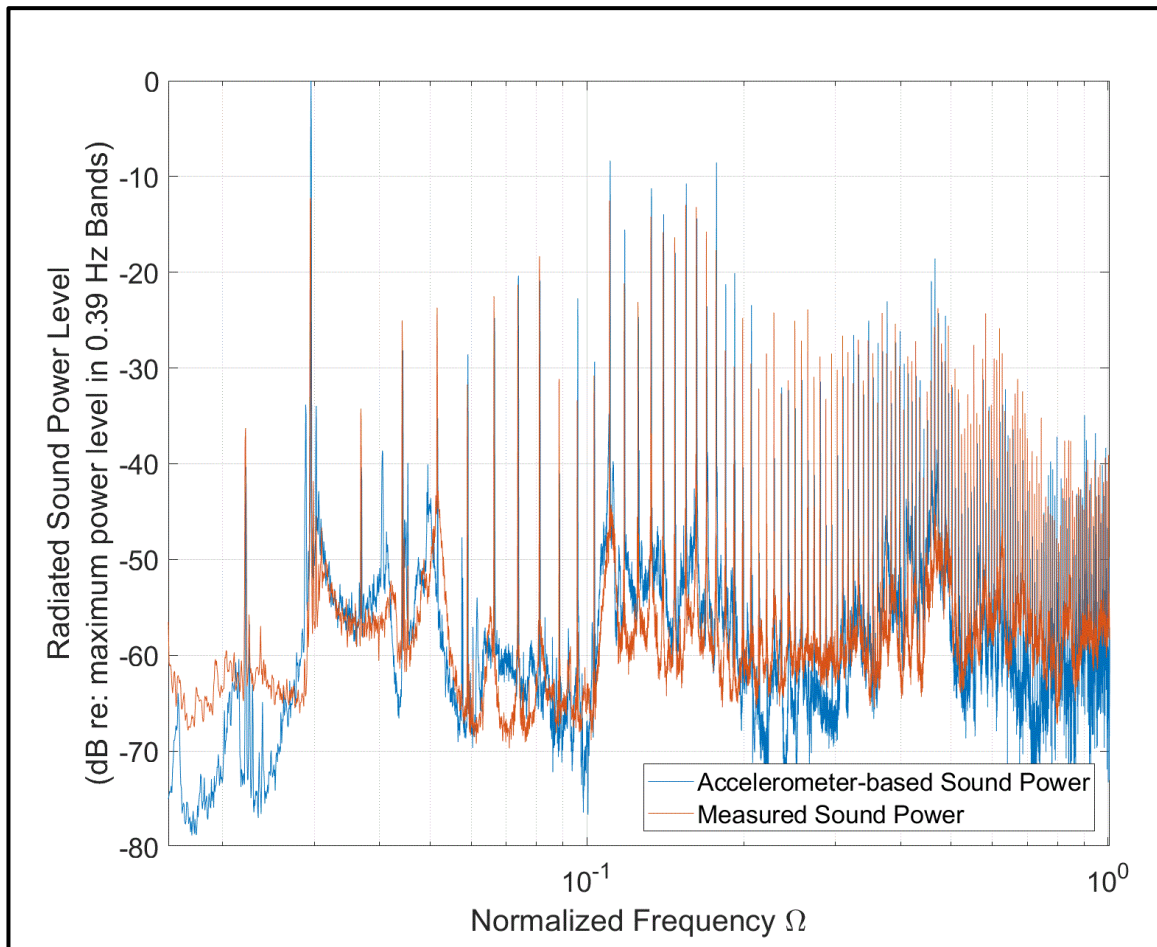


***Figure 3-16. Normalized radiated sound power level in 0.39 Hz bands. The blue line was calculated from the averaged sound power transfer function, surface-averaged acceleration, and measured surface acceleration during operation. The orange line was measured in accordance with the ANSI/ISO 3745:2012 standard.***

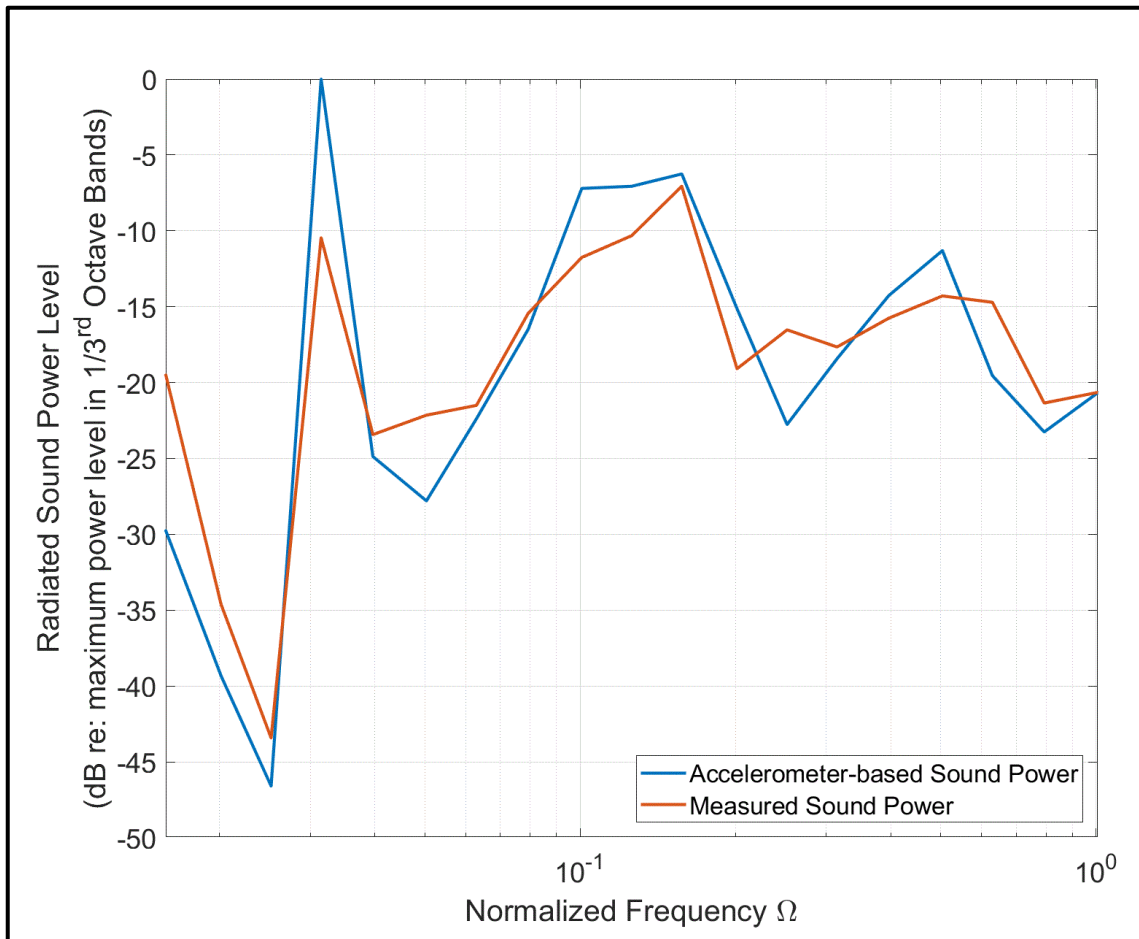


**Figure 3-17. Normalized radiated sound power level in one third octave bands. The blue line was calculated from the averaged sound power transfer function, surface-averaged acceleration, and surface acceleration during operation. The orange line was measured in accordance with the ANSI/ISO 3745:2012 standard.**

# Chapter 4

## Noise Control

### 4.1 Fundamental Design

Considering the results from the vibration and acoustic diagnostics work performed, it is clear that the main flaw of the design of record unit is the foundation upon which it is mounted. A close correlation between radiated sound power and transmissibility demonstrates the significance of the mechanical transmission path from the compressor to its housing. Mobility and modal analysis results reveal that the vibration isolation system is physically coupled to the most flexible parts of a modally rich structure. Finally, sound power transfer function measurements show that the modes directly excited by the spring mounts can efficiently radiate tones that reside within a frequency range that is easy for the average human to hear, resulting in an abundance of unwanted noise. In order to mitigate the mechanically transmitted noise, the vibration isolation must be grounded to a much stiffer base.

A fundamental solution was proposed to rework the suspension system so it can be mounted onto a rigid base and decoupled from the thin shell surrounding the compressor. Figure 4-1 shows a transparent structural model of the assembly designed for noise control testing. The compressor was hard mounted with cast steel cylinder blocks onto a cast steel secondary plate. Four springs with half the stiffness of the design-of-record mounting springs supported the compressor by the secondary plate. The springs were mounted to a thick steel plate, which had tapped holes that would allow for the assembly to be bolted down to the same fixture used for diagnostic transmissibility testing. Given the considerable increase in height, the lower housing was extended with welds in order to fit the compressor completely within the enclosure. The

purpose of designing such a drastic change to the structural system was to remove, or otherwise limit, the influence of shell modes on the mechanical transmission between the compressor and the housing.

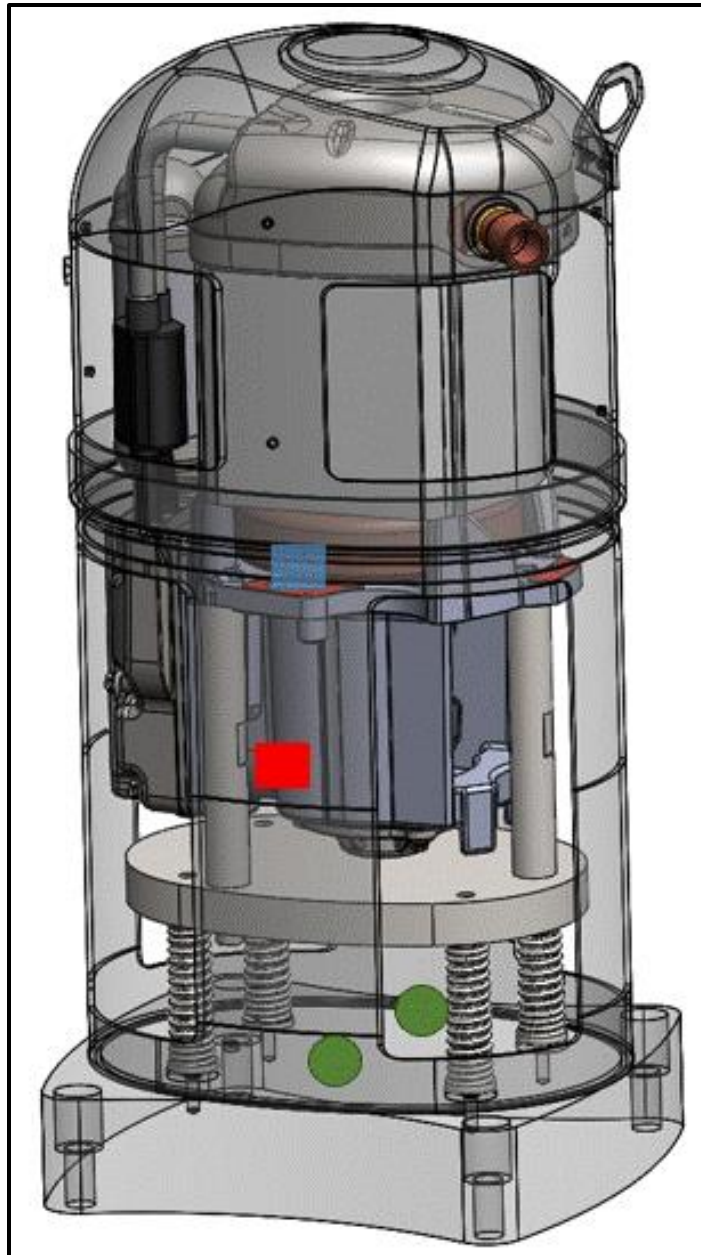


*Figure 4-1. Transparent schematic of the windowed compressor fabricated for noise control testing. Acceleration spectra were measured with triaxial accelerometers at the shell enclosure (red square) and the compressor crankcase (blue square). The experiment was controlled with two uniaxial accelerometers on the rigid base (green circles).*

## 4.2 Experimental Procedure

Figure 4-1 shows the locations of the primary accelerometers used to take measurements on the rigid-base compressor. The attenuation, defined as the linear reciprocal of the transmissibility, was measured between the compressor at one of the sides of the crankcase and the enclosure at the approximate relative location of the design of record spring mount. As with the previous shake testing, the foundation was shaken; vibrations were measured along three coordinate directions, shown in Figure 4-2; and the transmissibility theorem was used, allowing for the measurement of attenuation from the shell to the compressor. The same hardware and software for the transmissibility testing was used for the noise control testing.

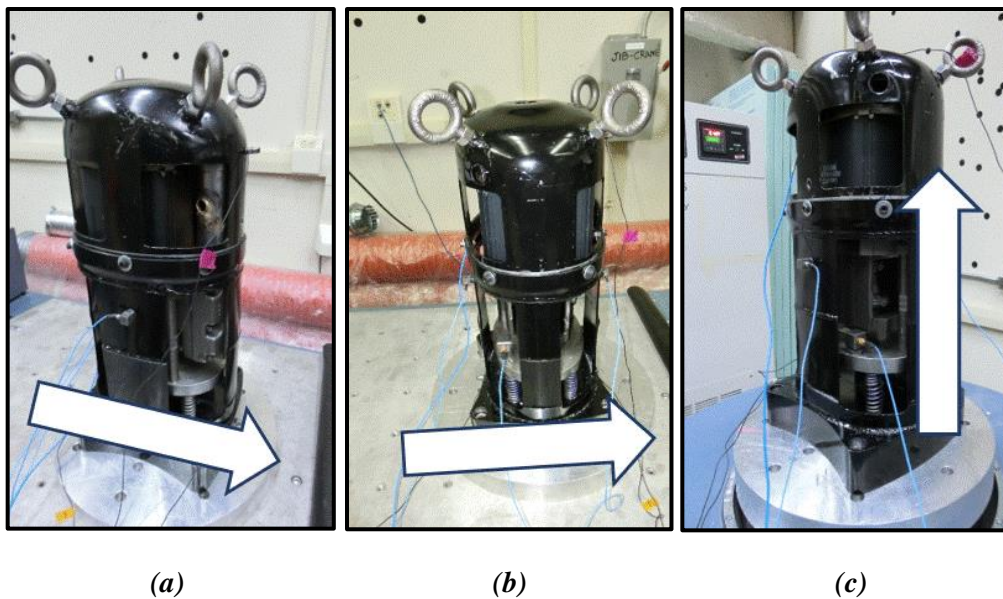


*Figure 4-2. Orientations of the rigid-base compressor on the shaker and slip table. The compressor was shaken in the X (a), Y (b), and Z (c) directions, as indicated by each arrow.*

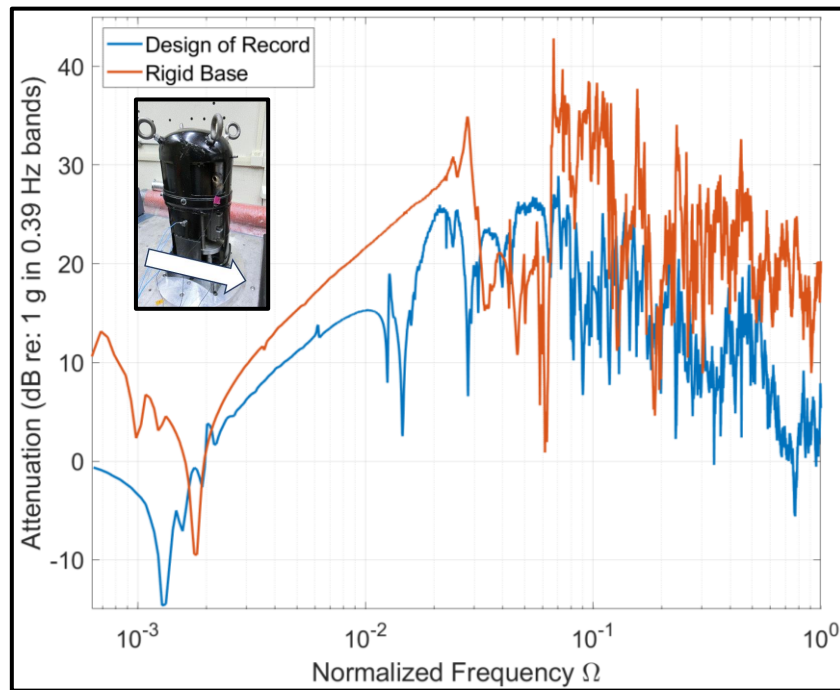
### 4.3 Results & Discussion

Figure 4-3 displays the attenuation in decibels between the enclosure and the compressor for mechanical vibration transmission in the X direction, as indicated by the arrow. The rigid base condition shows 5-15 dB more attenuation than the design of record condition at most frequencies; however, there is one trough at  $\Omega = 0.06$  that raises some concern. This local minimum, along with others found at  $\Omega = 0.14$  and  $\Omega = 0.19$ , notably deviates from the general improvement in the performance of the vibration isolation system, and it suggests that there may be a mechanical or structural property with unaccounted for resonances.

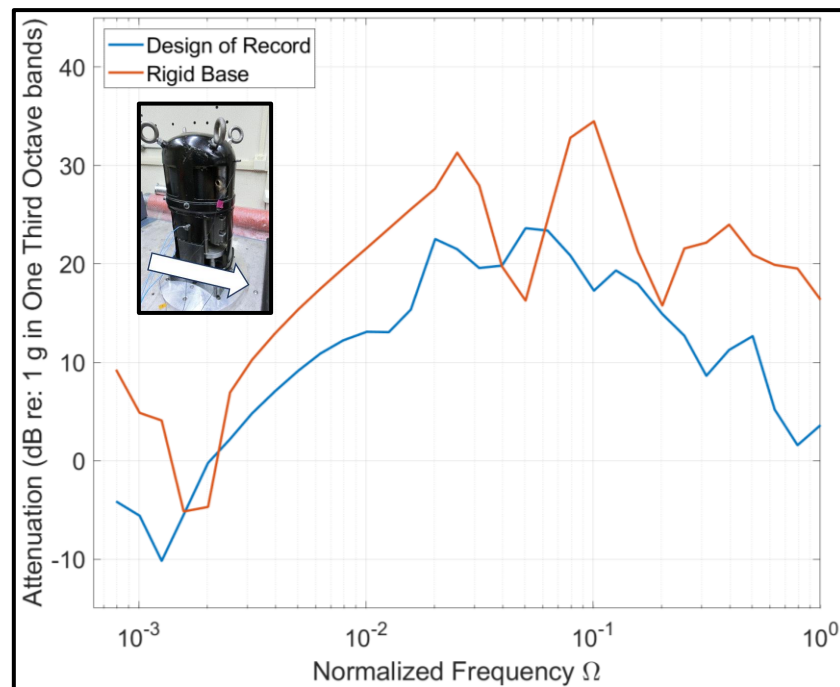
Figure 4-4, displaying the attenuation in the Y direction, shows similar results to those found for the X direction. The same minima for the rigid base condition are identified in the former as those discussed in the latter; however, they have 5-10 dB less influence on the narrow band spectrum. In fact, the attenuation measured for the rigid base condition is 5-15 dB greater than that of the design of record condition across the bulk of the frequency range shown, and the attenuation does not show signs of a steady decrease with increasing frequency. The shell has many modes with high mobility along surfaces normal to the Y direction; therefore, it is promising to see that mechanically-transmitted vibrations are mitigated well along this coordinate direction.

Figure 4-5 shows both the attenuation measured for the design of record and rigid base conditions in the Z direction. While the design of record unit's vibration isolation system starts to fail at  $\Omega = 0.06$ , the system used for the unit with a rigid base continues to perform well at frequencies above this value. As was observed for the other two directions, mechanical resonances are observed; more details on these resonances are discussed in the subsection on spring surging.

Overall, significantly greater attenuations were achieved with the rigid base configuration compared to the design of record configuration at nearly all frequencies and in all three coordinate directions. Particularly at higher frequencies, within the critical range of human hearing, it is evident that the influence of the structural characteristics of the shell is diminished after moving the spring mounts onto the rigid base. The significantly greater attenuation leads to the possibility for a decrease in radiated noise from an operable compressor with the same suspension system.

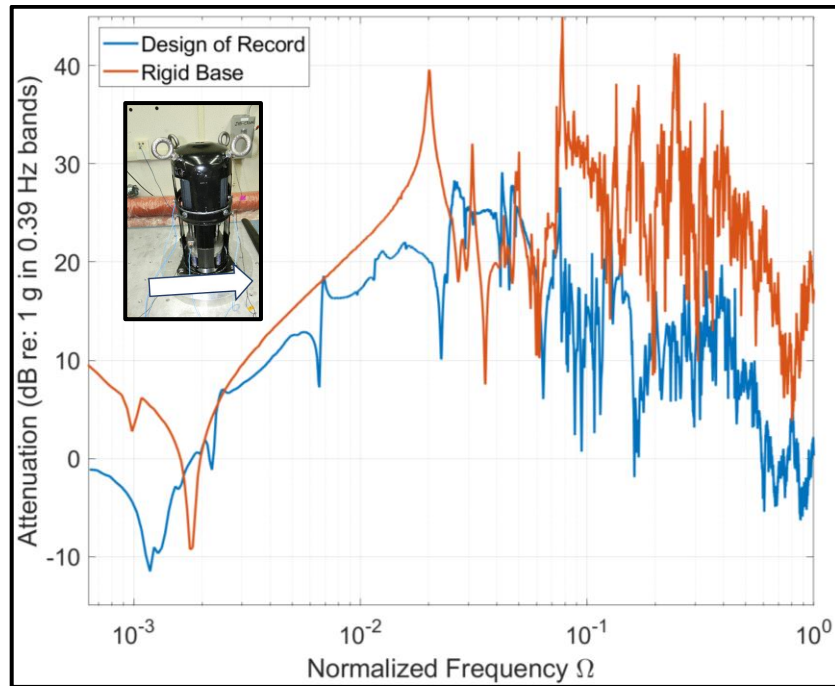


(a)

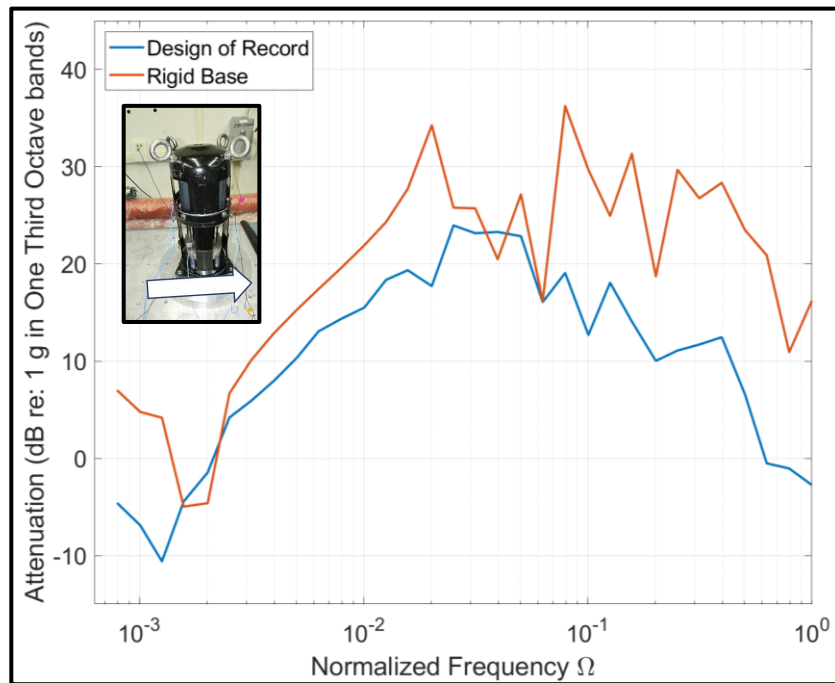


(b)

**Figure 4-3. Attenuation in (a) 0.39 Hz bands and in (b) one third octave bands from the surface of the enclosure at the original bottom spring mount location to the compressor crankcase, forced and measured in the X direction. The blue line in each graph represents the design of record compressor measurements; the orange line represents those taken on the rigid base assembly.**

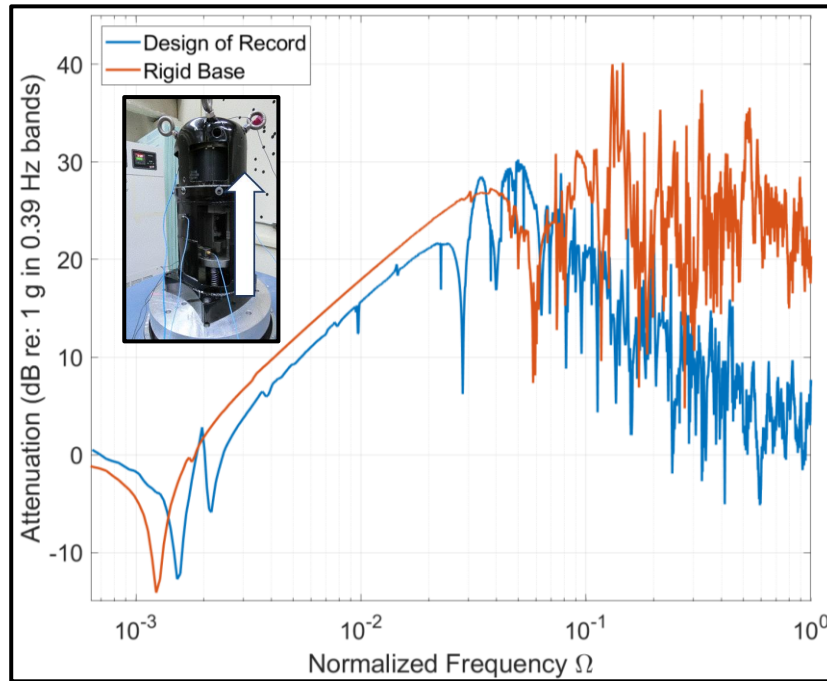


(a)

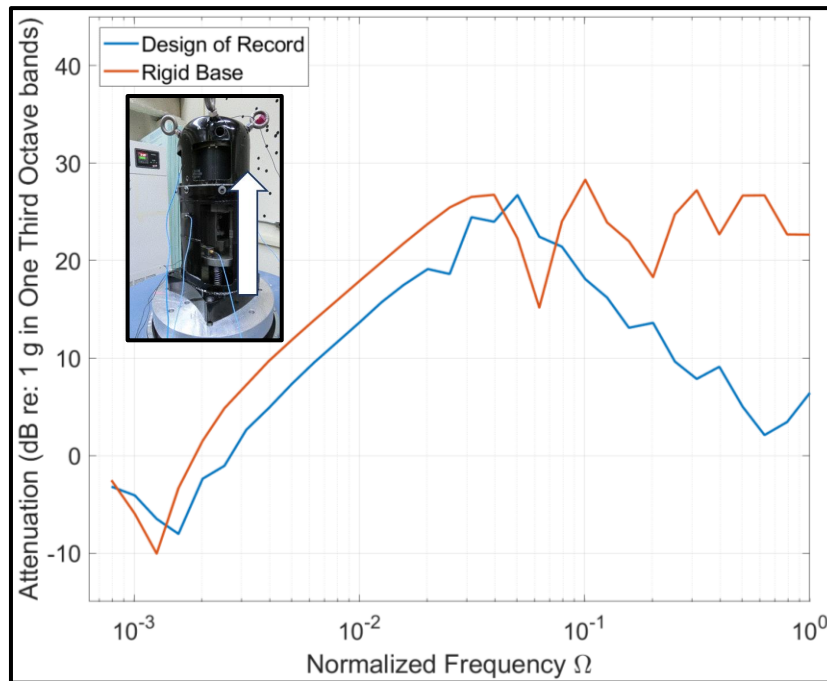


(b)

**Figure 4-4. Attenuation in (a) 0.39 Hz bands and in (b) one third octave bands from the surface of the enclosure at the original bottom spring mount location to the compressor crankcase, forced and measured in the Y direction. The blue line in each graph represents the design of record compressor measurements; the orange line represents those taken on the rigid base assembly.**



(a)



(b)

*Figure 4-5. Attenuation in (a) 0.39 Hz bands and in (b) one third octave bands from the surface of the enclosure at the original bottom spring mount location to the compressor crankcase, forced and measured in the Z direction. The blue line in each graph represents the design of record compressor measurements; the orange line represents those taken on the rigid base assembly.*

#### 4.4 Spring Surging

One compromising aspect of the vibration isolation system that has not been addressed thus far has been spring surging. This is a phenomenon that occurs when standing waves excite resonances within the springs themselves. The fundamental surge resonance and its harmonics can be calculated with the simple equation given by Shigley & Mitchell [19]

$$f_n = \frac{n}{2} \sqrt{\frac{sg}{W}} = \sqrt{\frac{s}{m}}, \quad (4-1)$$

where  $n$  is the frequency mode ( $=1,2,3,\dots$ ),  $s$  is the stiffness of the spring,  $m$  is the mass of the spring,  $g$  is the gravitational constant, and  $W$  is the weight of the active coils of the spring. The damping ratios for each resonance can be determined for in the same manner as the fundamental resonance of the single degree-of-freedom system.

Figure 4-6 shows the attenuation of the rigid base assembly along the Z direction. Single degree-of-freedom (1-DOF) models of attenuation (reciprocal of transmissibility, as calculated by Equation 2-9), with resonances at the spring surge frequency and its harmonics, were computed and added to a 1-DOF model with the fundamental mass-spring-damper resonance frequency. These calculations were performed to present the spring surging model, shown in black, which shows a clear picture of the behavior of the attenuation for at least 2-3 surge frequencies. The spring surging model proves useful in revealing the underlying reason for troughs in attenuation. Spring surge modeling was not attempted for the X and Y directions, for the springs are not

oriented in those directions. However, coating the springs with a form of damping suitable to treat spring surging will likely improve attenuation in all three coordinate directions.

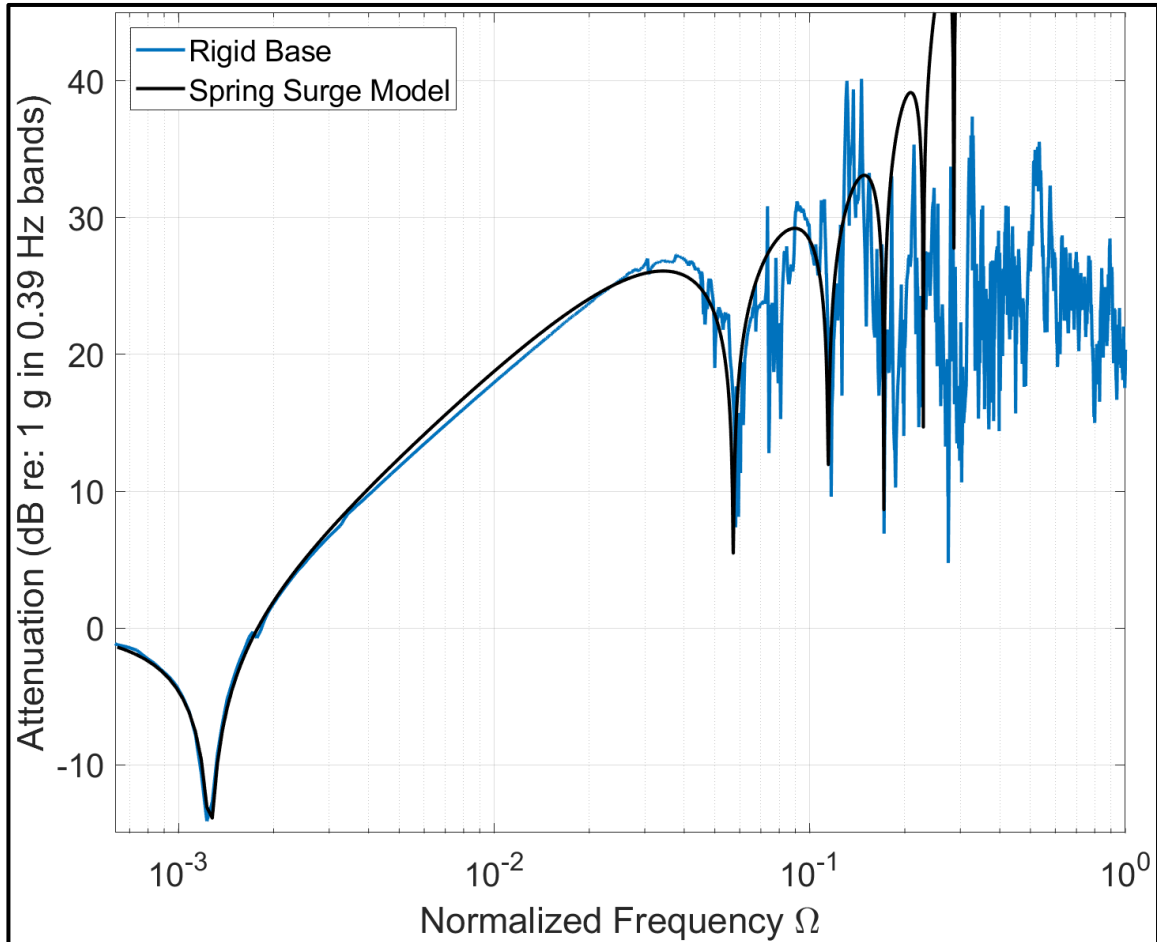


*Figure 4-6. Attenuation of rigid base assembly in Z-direction, compared to a 1-DOF model with spring surging resonances.*

# Chapter 5

## Summary and Recommendations for Future Work

The purpose of this thesis project was to determine the dominant transmission path of noise from a small, hermetic, reciprocating, refrigerant compressor; study this noise path to determine its primary issues; validate a noise monitoring method rooted in structural acoustics theory; and test a fundamental design solution to mitigate the noise issues.

The mechanical transmission path gained more focus than the acoustic path during these experiments. An ANSI/ISO standard was used to measure the radiated sound power level of an operating compressor unit in a controlled environment. Another standard published by ASHRAE was used to compare a production line unit to a compressor hard mounted to its enclosure. In addition, transmissibility of the suspension system of an inoperable compressor unit was measured with several changes to the vibration isolation, including a rigidly mounted condition that was compared to the design of record. It was soon learned that the difference in the radiated sound power spectra between the rigidly mounted and design of record compressor units was similar to the difference in vibration transmissibility between the rigidly mounted and design of record compressor units designed for transmissibility testing. Thus, understanding and attenuating the mechanical transmission path became the primary objective of further diagnostics and noise control efforts.

Mobility and modal analysis measurements were executed on a compressor primed for radiated sound power testing. The results of these experiments revealed information that strengthened the argument for the increased focus on treating the mechanical noise path. The surface-averaged mobility curves of the contact areas of the spring mounts contain dominant peaks that correlate well with cylindrical mode shapes found in the modal analysis, raising a

strong possibility that the compressor is mounted to a flexible, non-rigid foundation at its most mobile parts, and the compressor excites a plethora of structural shell modes within the critical range of human hearing, simply by being vibrationally coupled to the shell at antinodal regions of these modes.

The measurement of the sound power transfer function, taken using the same microphone array and room as the initial sound power level measurement, served the purposes of evaluating the radiation efficiency of the shell modes found in the modal analysis, determining how well different surfaces of the housing radiate sound, and constructing a sound power per surface-averaged vibration function to be used to monitor noise. It was learned that the cylindrical shell modes found in the modal analysis, and verified with mobility measurements, are highly efficient radiators of sound. The parts of the compressor enclosure with the least modal activity are the most inefficient at radiating sound, and the noise monitoring technique explored in this thesis is comparable to monitoring the sound source with microphones. While it is unfortunate to learn of the consequences of the compressor mounting design, it is encouraging to see a close relationship between the monitoring technique and the ANSI/ISO standard for obtaining radiated sound power spectra; this accelerometer method has the potential to facilitate the assessment of noise control treatments and design changes to manufactured products.

Finally, a successful attempt was made to attenuate the mechanical transmission path with a conceptually simple, albeit practically drastic, change to the design of the suspension system and its foundation. The results of this experiment show that decoupling the springs from the hermetic shell by grounding the system to a rigid base improves mechanical noise isolation. It is, therefore, recommended that the structural design of any heating, ventilation, and air conditioning (HVAC) appliance with an internal suspension system include this decoupling, that any vibrations generated by the engine are grounded through its vibration isolation mounts to a rigid foundation and not transferred to a compliant, modally dense surface.

Future assessment of this design should include the construction of an operable compressor with the suspension system evaluated in Chapter 4, as to measure radiated sound power level and compare to the design of record for validation of all the findings produced in this thesis. If the sound power level is sufficiently reduced with this new design, the concept should be retained, and a more practical solution be reached for a new iteration of the current product. In any case, it is also recommended that damping be applied to the bottom springs for treating spring surging as well as to the housing of the compressor to mitigate sound radiation at structural shell resonances.

## References

- [1] T. Nagao, H. Sasano, S. Yanase, J. Yabiki, H. Iwai and T. Ide, "Noise Reduction of a High Efficiency Reciprocating Compressor," in *International Compressor Engineering Conference*, 2000.
- [2] J. Hamilton, *Measurement and control of compressor noise*, West Lafayette, IN: Purdue University, 1988.
- [3] K. Tojo, S. Machida, S. Saegusa and T. Hirata, "Noise Reduction of Refrigerator Compressors," in *International Compressor Engineering Conference*, 1980.
- [4] M. P. Waser and J. F. Hamilton, "Noise Reduction of Hermetic Refrigeration Compressors by Changes of Hermetic Shell Characteristics," in *International Compressor Engineering Conference*, 1984.
- [5] Acoustical Society of America, "ANSI/ASA S12.55-2012 / ISO 3745:2012: Acoustics – Determination of sound power levels and sound energy levels of noise sources using sound pressure – Precision methods for anechoic rooms and hemi-anechoic rooms," American National Standards Institute, 2012.
- [6] J. H. Prout and R. C. Marboe, "ARL Penn State Flow-Through Anechoic Chamber," *ARL Penn State Technical Memorandum No. 89-65*, 22 February 1990.
- [7] ASHRAE , American Society of Heating, Refrigeration and Air Conditioning Engineering Applications Handbook, ASHRAE, 1999.

- [8] J. C. Snowdon, *Vibration and Shock in Damped Mechanical Systems*, New York: John Wiley and Sons, 1968.
- [9] L. Kinsler, A. Frey, A. Coppens and J. Saunders, *Fundamental of Acoustics*, 4th ed., New York: John Wiley and Sons, 2004.
- [10] Gardonio and Fahy, *Sound and Structural Vibration*, 2nd ed., Elsevier, 2007.
- [11] A. Leissa, *Vibrations of Shells*, Acoustical Society of America, 1993.
- [12] B. Berndt, *Ramanujan's Notebooks*, Berlin: Springer Verlag, 1985.
- [13] Cremer, Heckl and Ungar, *Structure-Borne Sound*, 2nd ed., Berlin: Springer, 1988.
- [14] S. Hambric and J. Fahline, "Structural Acoustics Tutorial: Part II," *Acoustics Today*, pp. 9-27, 2007.
- [15] R. Mindlin, "Influence of rotatory inertia and shear on flexural motions of isotropic, elastic plates," *ASME Journal of Applied Mechanics*, pp. Vol. 18 pp. 31-38, 1951.
- [16] G. Maidanik, "Response of ribbed panel to reverberant acoustic fields," *J. Acoust. Soc. Am.*, pp. 809-826, 1962.
- [17] Szechenyi, "Free vibration of cylindrical shells partially filled with liquid," *Journal of Sound and Vibration*, vol. 19, no. 1, pp. 65-81, 1971.
- [18] L. Beranek, *Acoustics*, New York, NY: American Institute of Physics, 1986.
- [19] J. E. Shigley and L. D. Mitchell, *Mechanical Engineering Design*, McGraw-Hill, 1983.

- [20] D. Ewins, *Modal testing: Theory and practice*, New York: John Wiley and Sons, 1986.